MX2 restricts HIV-1 and herpes simplex virus-1 by forming cytoplasmic biomolecular condensates that mimic nuclear pore complexes

George D. Moschonas[1,2], Louis Delhaye[1,3], Robin Cooreman[1,2], Anayat Bhat[7], Delphine De Sutter[1,3], Eef Parthoens[4,5,6], Anne-Sophie Desmet[1,2], Aleksandra Maciejczuk[1,3], Hanna Grzesik[1,3], Saskia Lippens[4,6], Zeger Debyser[7], Sven Eyckerman[1,3]* & Xavier Saelens[1,2]*

[1]VIB Center for Medical Biotechnology, VIB, Technologiepark-Zwijnaarde 75, 9052 Ghent, Belgium.

[2]Department of Biochemistry and Microbiology, Ghent University, Technologiepark-Zwijnaarde 75, 9052 Ghent, Belgium.

[3]Department of Biomolecular Medicine, Ghent University, Technologiepark-Zwijnaarde 75, 9052 Ghent, Belgium.

[4]VIB Center for Inflammation Research, Technologiepark-Zwijnaarde 71, 9052 Ghent, Belgium.

[5]Department of Biomedical Molecular Biology, Ghent University, 9052 Ghent, Belgium.

[6]VIB BioImaging Core, VIB, 9052 Ghent, Belgium.

[7]Department of Pharmacological and Pharmaceutical Sciences, Laboratory of Molecular Virology and Gene Therapy, KU Leuven, Herestraat 49, 3000 Leuven, Belgium.

* shared senior authorship

Correspondence should be addressed to Sven Eyckerman and Xavier Saelens

Abstract

Human myxovirus resistance 2 (MX2) can potently restrict HIV-1 and herpesviruses at a post-entry step by a process that requires MX2 interaction with the capsids of these viruses. The involvement of other host cell factors in this process, however, remains poorly understood. Here, we mapped the proximity interactome of MX2 revealing strong enrichment of phenylalanine-glycine (FG)-rich proteins related to the nuclear pore complex as well as proteins that are part of cytoplasmic ribonucleoprotein granules. MX2 interacts with these proteins to form multiprotein cytoplasmic biomolecular condensates that are essential for its anti-HIV-1 and -herpes simplex virus-1 (HSV-1) activity. MX2 condensate formation requires the disordered N-terminal region of MX2 and its dimerization. We also demonstrate that incoming HIV-1 and HSV-1 capsids associate with MX2 at dynamic cytoplasmic biomolecular condensates. Our results reveal that MX2 forms nuclear pore-mimicking cytoplasmic condensates that act as nuclear pore decoys, thereby interfering with nuclear entry of HIV-1 and HSV-1.

Vertebrate cells respond to type I interferon (IFN) by the induction of hundreds of IFN-stimulated genes (ISGs), which establishes an "antiviral state" in the cell[1,2]. One of the most intriguing ISGs is *Myxovirus Resistance* (*MX)*. Humans, like most mammals, have two *MX* paralogues named *MX1* and *MX2* and their gene products, named MX1 (or MxA) and MX2 (or MxB), can restrict a broad range of viruses[3]. MX2 exists in two isoforms, full-length MX2(1-715) and short isoform MX2(26-715) that lacks the first 25 N-terminal residues[4].

MX2 has been identified as a potent restriction factor of HIV-1 and other primate lentiviruses[5–7]. More recently, it was reported that MX2 can also suppress the replication of herpesviruses[8–13], Hepatitis C Virus (HCV)[14,15], and Hepatitis B Virus (HBV)[16]. In addition, MX2 has been implicated in mitochondrial integrity[17] and in the control of long interspersed element type 1 retrotransposition[18].

MX proteins belong to the dynamin superfamily of large GTPases[19]. The crystal structure of the MX2 dimer, without the first N-terminal 83 amino acids, has been resolved. This revealed that MX2 adopts an extended three-domain architecture with an N-terminal globular GTPase domain that is connected to a stalk domain by a bundle signaling element[20]. The GTPase domain enables GTP-binding and -hydrolysis, which, remarkably, is required for MX2 antiviral activity against herpesviruses and HBV but not for HIV-1 restriction[5,6,8,9,12,21]. MX2 oligomerization, at least as a dimeric assembly, and localization are major determinants of MX2 anti-HIV-1, -herpesviruses, and -HBV activity [8,9,16,20,22,23].

The N-terminal domain (NTD) of MX2 is also a key determinant for MX2 antiviral activity[24]. The first 25 residues contain a nuclear localization signal (NLS) that targets MX2 to the nuclear membrane and a triple arginine motif that facilitates HIV-1 capsid binding[21,25,26]. The NTD, however, also harbors a disordered region (amino acids 26-90) that is crucial for MX2 localization and HIV-1 and HBV antiviral activity[16,21].

Proteins with disordered regions are prone to undergo so-called liquid-liquid phase separation (LLPS), a compartmentalization process that is associated with the formation of biomolecular condensates and membraneless organelles (MLOs) in a cell[27–29]. Biomolecular condensates are characterized by a region of highly concentrated proteins and, often, nucleic acids, and they can rapidly exchange material with their surroundings, dissipate, and reassemble[30,31].

Here we used a proximal labeling method to identify interaction partners of MX2 and demonstrate that LLPS is an essential process in MX2-mediated restriction of HIV-1 and HSV-1.

Results

MX2 interacts with FG-rich nuclear pore protein subunits and granule-associated ribonucleoproteins

To identify dynamic MX2 protein partners, we performed proximity-dependent biotin identification (BioID) using TurboID, a highly active promiscuous biotin ligase[32,33]. Full length MX2(1-715) was genetically fused with TurboID through a T2A self-cleaving site for control conditions (MX2 and TurboID expressed as separate proteins), and through a mutant T2A (MUTT2A) linker for the experimental condition (MX2 fused to TurboID)[34] (S Fig.1a). The functionality of the MX2-MUTT2A-TurboID fusion construct was assessed in transient transfection experiments, which confirmed its capacity to dimerize with co-expressed MX2(1-715), its ability to restrict HSV-1, and its localization at the nuclear membrane (Supplementary Fig.1b-d).

Next, we generated two U87-MG cell lines which, upon low dose doxycycline stimulation, expressed either MX2 and TurboID as separate (MX2-T2A-TurboID) or fused (MX2-MUTT2A-TurboID) proteins, together with untagged MX2. This ”T2A split-link design” ensures equal biotin ligase activity in both cell lines (Supplementary Fig.2a). We then performed BioID experiments with these pairs of cell lines under three conditions: (i) doxycycline-treated (-IFN), (ii) doxycycline-treated combined with IFNa2a stimulation (+IFN), and (iii) doxycycline-treated and infected with HSV-1 (HSV-1) (Supplementary Fig.2b). Our T2A split-link design resulted in comparable MX2 differential enrichment in all three conditions, thereby supporting sensitive differential analysis (Supplementary Fig.2c).

Using this proximity labeling approach we identified nearly all previously reported MX2-interacting proteins[35,36]. We also identified novel, highly enriched, MX2-interacting candidates that are known to localize at the nuclear pore or in the cytoplasm (Fig.1a) (Supplementary Table.1). There were 253 proteins enriched in all three conditions (Fig.1b) (Supplementary Table.2). A subset of these proteins are known to participate in nuclear transport and are part of or interact with the nuclear pore complex (NPC). This nuclear pore network includes novel MX2-interacting candidates such as NUPL1(NUP58), NUP54, NUP35, and nuclear transport receptor transportin-2 (TNPO2), which were highly enriched in the interactome screen. Unexpectedly, however, a large fraction (106 proteins) of the common enriched proteins are known to participate in the regulation of translation and RNA catabolic processes and are part of ribonucleoprotein (RNP) granules with LLPS properties (Fig.1b and Supplementary Fig.3a).

The common candidate MX2-interacting proteins also included mitochondrial and coated vesicle proteins (Supplementary Fig.3b, c) (Supplementary Table.2).

The nuclear pore network consists of nucleoporins (Nups), which are structural components of the NPC, and nuclear transport factors (Fig.1c). The enriched nuclear transport factors were primarily importin-beta family proteins, while importins-alpha, their heterodimeric partners in the nuclear cargo translocation system, were poorly enriched and not consistently identified (Fig.1c-e). MX2 was reported to localize at the cytoplasmic face of the nuclear pore[35]. The cytoplasmic outer ring components NUP133, NUP85, and NUP107, however, were the least enriched Nups, while Nups that form part of the central channel (e.g. NUPL1), cytoplasmic filaments (e.g. RANBP2), inner ring (e.g. NUP35), and even the transmembrane ring of the NPC (e.g. POM121) were highly enriched (Fig. 1c, d). These highly enriched Nups comprised phenylalanine-glycine (FG)-rich Nups of the human NPC[37] (Fig. 1d, f). This was a striking observation because FG-Nups have phase separation qualities, a property shared with inner ring Nup NUP35[38,39].

The ribonucleoprotein granule network, on the other hand, consists of RNA-binding and disordered domain-containing proteins that are present in cytoplasmic MLOs, specifically in processing bodies (PBs) and stress granules (SGs) (Fig. 1g-i and Supplementary Fig.3d). SAMD4B, FAM120C, SAMD4A, FUBP3, and TRIM56 were among the more enriched of these ribonucleoprotein granule network proteins in all three conditions (Fig. 1g). SAMD4A forms granular cytoplasmic LLPS condensates, known as Smaug1 condensates, that are distinct from PBs and SGs[40]. This MX2-interaction network overlapped substantially with a reported PB subnetwork, supporting the validity of our proximity labelling approach[41] (Fig.1j) (Supplementary Table 3).

In summary, our proximity interactome analysis suggests that MX2 interacts with FG-rich region(s) components of the NPC and with cytoplasmic granule-associated ribonucleoproteins.

HIV-1 and HSV-1 inhibition by MX2 involves SAMD4A, TNPO1, and NUP35, whereas NUP62 is dispensable for HSV-1 but not for HIV-1 restriction

We performed RNA interference (RNAi) experiments to address the possible functional importance of identified candidate MX2-interacting proteins on MX2-mediated restriction of HIV-1 and HSV-1 using doxycycline-inducible MX2 HeLa cells (Supplementary Fig.4a). We selected a total of 12 genes based on enrichment in our screening and/or their reported HIV-

1 or HSV-1 capsid (CA) binding properties during viral entry (Supplementary Fig.4b). Knockdown (KD) of SAMD4A, TNPO1, and NUP35 impaired MX2-mediated restriction of HSV-1 and HIV-1 with NUP35 having a more modest influence on the HSV-1 restriction. KD of NUP62, a central channel Nup known to interact with the HIV-1 but not HSV-1 CA, only affected HIV-1 restriction[42,43] (Fig.2a, b and Supplementary Fig.4c). The observations for TNPO1, SAMD4A, and NUP35 were confirmed by multiple round infection with an HSV-1 C12 GFP reporter strain and no additive effects were observed by KD of two target genes simultaneously (Fig.2c). The importance of TNPO1, SAMD4A, and NUP35 for the MX2 antiviral activity was confirmed in single round infection experiments with HSV-1 and HIV-1 with combined KD of two genes in each condition (Supplementary Fig.4d and e). Thus, TNPO1 and SAMD4A play a critical role in MX2-mediated restriction of both HIV-1 and HSV-1, NUP35 has a modest impact on the anti-HSV-1 and a more pronounced effect on the anti-HIV-1 activity of MX2, while NUP62 KD only affects the anti-HIV-1 activity of MX2.

MX2 interacts with SAMD4A, TNPO1, and NUP35 at dynamic cytoplasmic biomolecular condensates

We next performed high resolution confocal fluorescent microscopy experiments to identify the subcellular compartments where MX2 resides and how its localization might be affected by identified interaction partners. In line with earlier reports, MX2 localized at the nuclear membrane and in cytoplasmic puncta[44] (Fig.3a). The interaction between MX2 and SAMD4A, TNPO1, and NUP35 was confirmed using the NanoLuc Binary Technology (NanoBiT), a protein complementation assay (Fig.3b). We then performed confocal microscopy to reveal the cellular compartments where these proteins might colocalize with MX2. SAMD4A was observed in MX2-containing puncta in the presence of MX2 while still forming distinct SAMD4A-containing condensates[45]. MX2 changed the diffuse cytoplasmic expression pattern of TNPO1 with the two proteins colocalizing at the nuclear membrane and in cytoplasmic MX2 puncta. Similarly, in the presence of MX2, NUP35 relocated to MX2 cytoplasmic puncta (Fig.3c).

Next, we performed live cell-imaging to study the properties of the MX2-containing puncta in MX2-EGFP expressing HeLa cells. The MX2 puncta turned out to be highly dynamic and coalesced to form larger condensates. This suggests that MX2 undergoes LLPS to become enriched in cytoplasmic biomolecular condensates, some of which were also associated with the nuclear envelope (Fig.3d and sup. video.1). Live cell imaging was also performed for all

three EGFP-tagged MX2-interacting proteins in the presence of mScarlet-tagged MX2. SAMD4A colocalized with the MX2 condensates and, also, presented as SAMD4A-containing Smaug1 condensates that were adjacent to MX2 condensates. Similarly, TNPO1- and NUP35-positive MX2 condensates were observed that fused with each other (Fig.3e, Supplementary Fig.5a, and sup. videos.2-4). Using confocal microscopy, we then assessed the cytoplasmic colocalization of MX2 with SAMD4A, TNPO1, and NUP35 and found that all four proteins are components of the same cytoplasmic condensates. Remarkably, MX2 showed a distinct outer face ring-like pattern suggesting spatial heterogeneity in the condensates (Fig.3f and Supplementary Fig.5b). Biomolecular condensates can have distinct material states including liquid, hydrogel, liquid crystal, and more solid-like amyloid-like fibrils that can be distinguished by their fluidity and (ir)reversible assembly[46]. We performed fluorescent recovery after photobleaching (FRAP) to confirm the high exchange rate of protein constituents which marks biomolecular condensates. We observed variation in FRAP plateaus, which likely reflects the different physicochemical properties of the constituent proteins. For EGFP-tagged MX2, FRAP reached a plateau of 39% reconstitution in 100sec. Notably, in the presence of TNPO1-mScarlet, MX2-EGFP signal recovery was increased, suggesting a higher fluidity (Fig.3g, h and Supplementary Fig.5c). Collectively, these data show that MX2 forms dynamic cytoplasmic biomolecular condensates that comprise SAMD4A, TNPO1, and NUP35.

MX2 assembles FG-Nups and importin-beta transporters at cytoplasmic biomolecular condensates

The observed outer ring-like pattern of MX2 and the intermediate MX2 FRAP rate suggest that MX2 forms a distinct subcompartment with low fluidity at the surface of the biomolecular condensates. Our proteomics data suggested that MX2 preferentially interacts with FG-Nups and with importin-beta transporters. FG-Nups create a selective NPC permeability barrier and can spontaneously self-assemble into dense hydrogels with NPC-like permeability[47,48]. Importin-beta transporters, on the other hand, have multiple FG-binding pockets that facilitate the rapid transfer of their cargo into the nucleus[49,50]. We hypothesized that MX2 could promote the assembly of FG-Nups to create an NPC-mimicking LLPS compartment in the cytoplasm. To test this hypothesis, we selected NUPL1 to represent FG-Nups and IPO4 as another importin-beta representative. NUPL1 overexpression induced cytoplasmic condensates even in the absence of MX2 (Fig.4a). In the presence of MX2, NUPL1-positive condensates colocalized with the previously observed condensates with MX2 distributed in an outer ring-like pattern (Fig.4a). The diffused cytoplasmic distribution of IPO4, however,

completely changed in the presence of MX2 with IPO4 relocating at the MX2 condensates (Fig.4a). A closer look at the NUPL1 and MX2 double positive condensates revealed that NUPL1 and MX2 both assembled at the outer face of the condensates (Fig.4b). The FG-Nups outer face of the MX2 condensates was also observed in the presence of IPO4 and was maintained during the fusion process implying a strong outer face predisposition (Fig.4c). In live cells, EGFP-tagged NUPL1 and mScarlet-tagged MX2 co-localized at the surface of fusion-competent condensates, while IPO4-positive MX2 condensates were also observed fusing in the cytoplasm and interacting with MX2 at the nuclear membrane (Fig.4d and sup. video.5,6). Additionally, the rapid signal recovery after photobleaching of IPO4 confirmed that importin-beta transporters interact with low affinity with FG-Nups and thus can easily cross the rim of the MX2 condensates in a similar way as they traverse the NPC barrier. NUPL1's and MX2's lower fluidity compared to IPO4 indicates a more gel-like phase separation material state of the cytoplasmic boundary of the condensates (Fig.4e).

MX2 cytoplasmic biomolecular condensates associate with other cytoplasmic MLOs and contain RNA-binding and disordered domain proteins

The second cluster of proteins in our proteomics data showed an association of MX2 with components of ribonucleoprotein granules that have LLPS properties such as PBs and SGs. Additionally, as shown above, SAMD4A, which contains both disordered and RNA-binding domains, participates in both the anti-HIV-1 and -HSV-1 activity of MX2 and interacts with MX2 at cytoplasmic condensates also in the form of distinct Smaug1 condensates. These data prompted us to evaluate the possible association of MX2 condensates with PBs and SGs. We selected LSM14A (identified in the MX2 BioID) and G3BP1 (not identified in the MX2 BioID) as respective marker proteins of these MLOs[41]. In both fixed and live cells, LSM14A was detected within the MX2 condensates while mainly visible as separate LSM14A-containing PBs that were in close proximity of and interacting with MX2 condensates (Supplementary Fig.6a, b and sup. video.7). In contrast, the diffuse cytoplasmic pattern of G3BP1 was not altered in the presence of MX2. However, after arsenite-induced stress, G3BP1 localized, as expected, into SGs and MX2 was observed in close proximity of or overlapping with these SGs (Supplementary Fig.6c).

To further unravel the composition and properties of the MX2 cytoplasmic biomolecular condensates, we selected proteins with disordered and/or RNA-binding domains that were highly enriched in our proteomics screen but did not affect MX2 antiviral activity upon

knockdown, *i.e*. SAMD4B, FUBP3, and CNOT4. These proteins colocalized with MX2 and NUPL1 in cytoplasmic condensates (Supplementary Fig.6d-e) that dynamically moved around in the cytoplasm and rapidly fused with each other (Supplementary Fig.6f and sup. videos.8,9). Furthermore, SAMD4B and FUBP3 displayed rapid FRAP reconstitution, suggesting their compartmentalization in a subcompartment of the MX2 condensates with high fluidity and liquid-like properties (Supplementary Fig.6g).

These results suggest that MX2 cytoplasmic condensates are multiprotein and heterogenous molecular assemblies that can associate with other MLOs.

The N-terminal disordered domain and dimerization of MX2 are required for cytoplasmic condensate formation

MX2 could play various roles in the condensate formation process functioning as a driver, regulator, or client. If MX2 acts as a driver, certain regions within its sequence must facilitate the required molecular interactions. To understand which domains of MX2 control its capacity to form condensates, we performed *in silico* analysis of the MX2 primary structure using four different prediction tools, dSCOPE[51], FuzDrop[52], IUPred2A[53], and PLAAC[54]. All tools predicted that the N-terminal regions 23-54 and 64-87 would be responsible for the MX2 phase separation properties (Fig.5a and Supplementary Fig.7a-c).

We generated 8 doxycycline-inducible HeLa cell lines with different V5-tagged MX2 mutants to assess the impact of the N-terminal part of MX2, the GTP-binding and -hydrolysis, and MX2 oligomerization on its localization and antiviral activity (Fig.5a and Fig.5b). The short MX2(26-715) isoform and MX2(51-715) failed to restrict HIV-1 and HSV-1 and, importantly, presented with a diffuse cytoplasmic expression pattern with few large condensates (Fig. 5c, d). The MX2(Δ26-90) mutant that maintained the first 25 amino acids but lacked the two predicted phase separation regions was also unable to restrict either virus. Despite the intact NLS, MX2(Δ26-90) displayed reduced nuclear membrane localization and formed highly dynamic condensate-like structures which were, however, unable to coalesce into larger condensates, pointing to an aggregate-like state (Fig. 5c-e and sup. video.10). In contrast, MX2(Δ26-50), which still contains the second more prion-like region (Supplementary Fig.7c), regained full antiviral activity and the ability to form condensates (Fig. 5c-e).

We also evaluated full length MX2 with well-defined point mutations since enzymatic activity and oligomerization strongly determine MX2's antiviral properties. The GTP-binding defective mutant MX2(K131A) was active against HIV-1 but not HSV-1 and formed condensates. Closer

inspection revealed that MX2(K131A) condensates had a different morphology compared to those formed by MX2 GTPase active mutants with a more equal distribution of the MX2 intensity and a less intense outer ring-like pattern (Fig.5f). Dimerization is important for MX2 antiviral activity and localization as shown by the monomeric interface 2 mutant MX2(M574D). MX2(M527D) did not inhibit either virus and had a completely altered localization with a diffuse nuclear and cytoplasmic pattern maintaining some localization in the nuclear membrane. The dimeric interface 1 mutant MX2(M666D) maintained similar properties as MX2(1-715) (Fig.5c-f and Supplementary Fig.7d-e). Similar localization patterns were confirmed by overexpressing EGFP-tagged MX2 mutants in HeLa cells. This included MX2(T151A), which can bind but not hydrolyze GTP. MX2(T151A) had a strong nuclear membrane accumulation and maintained the ability to form cytoplasmic condensates (Supplementary Fig.7f and sup. videos.10-18). Taken together, MX2 acts as the driving force behind biomolecular condensation, which requires its N-terminal disordered region and dimerization for the formation of biomolecular condensates and the restriction of HIV-1 and HSV-1.

TNPO1 and SAMD4A regulate the phase separation properties of MX2

We next tested the ability of MX2 mutants to bind TNPO1, SAMD4A, and NUP35 using the NanoBiT assay. MX2(26-715) and MX2(51-715), which lack the first 25 amino acids containing the NLS and the triple arginine motif, were unable to bind TNPO1, similar to the MX2(Δ26-90) mutant, which lacks the ability to form cytoplasmic condensates. SAMD4A had a higher binding affinity to the MX2(K131A) and MX2(M574D) compared to the other MX2 mutants (Fig.5g). We then generated a doxycycline-inducible HeLa MX2(1-715)-EGFP cell line to investigate the influence of TNPO1, SAMD4A, NUP35, and NUP62 on MX2 localization and condensate formation, aiming to comprehend the potential role of these MX2 interaction partners in regulating MX2 cytoplasmic condensate formation (Supplementary Fig. 8a). KD of TNPO1 reduced the nuclear accumulation of MX2 and the number of condensates by forming large condensates. Depletion of SAMD4A had no effect on MX2 nuclear accumulation, but resulted in a lower number of cytoplasmic condensates which were also smaller in size. NUP35 and NUP62 KD did not alter the nuclear membrane localization of MX2 or condensate formation (Fig. 5h). Taken together, both TNPO1 and SAMD4A affected MX2 biomolecular condensate formation which, for TNPO1, was dependent on MX2 N-terminal motifs.

MX2 condensates mimic the NPC LLPS environment to interact with incoming HIV-1 and HSV-1 capsids

MX2 restricts HIV-1 and HSV-1 by preventing nuclear entry of their genome[12]. To gain insights about the potential impact of the MX2 condensates on this mechanism, we visualized HIV-1 and HSV-1 incoming capsids in the presence or absence of wt and mutant MX2. For HIV-1, we used doxycycline-inducible HeLa MX2(1-715), -(26-715), and -(T151A) EGFP-tagged cell lines (Supplementary Fig.8a-c). MX2(1-715) and MX2(T151A) but not MX2(26-715) generated cytoplasmic condensates that trapped incoming HIV-1 capsids. We also observed HIV-1 capsids retained inside nuclear membrane-associated MX2 condensates (Fig.6a and Supplementary Fig.9a and b). Additionally, we infected HeLaP4 cells transiently expressing MX2-mScarlet with HIV IN-EGFP and followed single viral functionally active pre-integration complexes (PICs) during infection by visualizing the fluorescently labelled HIV-1 integrase (IN). Nuclear entry of HIV-1 PICs was prevented, and we observed EGFP signal inside cytoplasmic MX2 condensates (Fig.6b and Supplementary Fig.9c).

Imaging analysis of doxycycline-inducible V5-tagged MX2(1-715), (26-715), and (K131A) HeLa cell lines infected with HSV-1 revealed that only MX2(1-715) could prevent incoming HSV-1 capsids from reaching the nuclear membrane. HSV-1 capsids colocalized with MX2(1-715) condensates at the boundary between the condensates and the cytoplasm, and thus seemed to be unable to penetrate the surface of these condensates. HSV-1 CA that did not colocalize with MX2 were also observed in the cytoplasm of the HeLa MX2(1-715) cells (Fig.6c and Supplementary Fig.9d).

The distinct pattern of HIV-1 and HSV-1 capsid association with MX2 condensates resembles the distinct properties of nuclear entry of these two viruses. HIV-1 capsids can dock at the NPC cytoplasmic filaments (NUP358) and then, by interacting with Nups of the central channel (NUP62) and nuclear basket (NUP153), can reach the nucleoplasm[43,55–57] (Fig.6d). In contrast, HSV-1 capsids, facilitated by importins-beta, dock at the cytoplasmic face of the NPC (NUP358, NUP214, NUPL2) and subsequently release their genome through the NPC, leaving the empty capsid behind in the cytoplasm[42,58] (Fig.6e).

MX2 condensates interact with incoming HIV-1 and HSV-1 capsids at different steps of their journey towards the nucleus

We found that MX2 condensates interact with HIV-1 and HSV-1 capsids in the cytoplasm. Both viruses typically exploit the host microtubule (MT) cytoskeleton for long-range transport towards the nucleus[42,59]. We investigated whether the MX2 condensates, similar to other cytoplasmic MLOs[60], can use the MT network to move in the cytoplasm, possibly facilitating their encounter with viral capsids that travel along the MTs. MX2 condensates colocalized with MTs, indicating their capability to move along these structures (Fig.6f and Supplementary Fig.10a).

To further explore the role of MTs in MX2's anti-HIV-1 and HSV-1 restriction, we depolymerized the MT network with nocodazole. This treatment did not affect MX2's nuclear membrane localization, condensate formation, or distribution (Supplementary Fig.10b). In the case of HIV-1, as expected, the levels of infection remained unaffected in nocodazole treated cells, since HIV-1 particles have been shown to localize to nocodazole-resistant stable MTs[61]. However, the ability of MX2 to restrict HIV-1 infection decreased following the gradual disruption of the MT network (Fig.6g and Supplementary Fig.10c). In contrast, depolymerization of MTs had a greater impact on the ability of HSV-1 to reach the nucleus, consistent with previous reports[62,63]. Surprisingly, MX2's ability to hinder HSV-1 infection increased with increasing nocodazole concentrations (Fig.6h). These results suggest that MX2 condensates interact with HIV-1 capsids during their travel through the MT network and with HSV-1 capsids at a different step of their journey towards the nucleus.

Following entry, HSV-1 capsids utilize MTs and MT motors to reach the centrosome. From there, they translocate to the NPCs where they dock to FG-rich cytoplasmic filaments facilitated by nuclear transport factors, primarily importins-beta[42,64,65]. We previously observed a significant accumulation of importins-beta in the MX2 condensates and decided to investigate which properties of MX2 are responsible for that association. Our findings indicate that both MX2(T151A) and MX2(K131A) can generate condensates with accumulated IPO4 (an importin-beta), similar to MX2(1-715). However, the small number of large condensates generated by MX2(26-715) did not affect the diffuse cytoplasmic pattern of IPO4. According to these data, the delocalization of importins-beta is independent of GTP-binding and -hydrolysis but is controlled by the first 25 (NTD) residues of MX2 (Fig.6i and Supplementary Fig.10d).

Discussion

MX2 can restrict HIV-1 and herpesviruses, two highly divergent viruses, which involves common as well as distinct mechanistic features. Despite a large body of literature, the underlying mechanisms of MX2's antiviral activity remain largely elusive, although evidence for the involvement of additional host proteins is increasing[12]. Here, we mapped the proximal interactome of MX2 using an optimized T2A split-link design BioID method to help unravel the MX2 antiviral mechanism.

Detailed analysis of MX2's proximity interactome revealed strong enrichment of two protein clusters: FG-domain related nucleocytoplasmic transport components and cytoplasmic granule-associated ribonucleoproteins. Remarkably, both protein clusters have a high propensity to organize and function at LLPS compartments.

Earlier studies demonstrated that FG-rich Nups from different nucleopore subcomplexes are involved in the MX2 anti-HIV-1 activity and different Nup subcomplexes play a role in HIV-1 infection, MX2 activity and localization[35,55]. Several of those Nups such as NUP62, NUP153, NUP88, NUP98, and NUP358(RANBP2) can bind HIV-1 capsids and participate in the MX2 anti-HIV-1 activity[35,43,55,56]. We expanded the knowledge of cellular factor involvement in the MX2 antiviral activity against both HIV-1 and HSV-1. We identified SAMD4A, TNPO1, and NUP35 as significant contributors to MX2-mediated restriction of these viruses. Among these factors, NUP35 primarily affected the anti-HIV-1 activity, while NUP62 influenced only the anti-HIV-1 activity of MX2. Unlike NUP62, NUP35 does not directly bind to HIV-1 or HSV-1 capsids or participate in the nuclear entry of their viral genome. However, NUP35 interacts with other capsid-binding FG-Nups and therefore its enhanced impact on MX2's anti-HIV-1 activity can be explained by its stronger association with the HIV-1 capsid-binding NUP62[38].

SAMD4A, TNPO1, and NUP35 associated with the punctate cytoplasmic fraction of MX2. While expression of MX2 has been shown to form cytoplasmic structures[20,21,44,55], often referred to as puncta[11,17,25,26], the protein content or protein dynamics of these cytoplasmic structures were not studied. Supported by proteomics data, co-localization data, live cell imaging, and FRAP, we now firmly establish that MX2 forms dynamic cytoplasmic biomolecular condensates. MX2 condensates are multiprotein and heterogenous, comprised of FG-rich Nups and RNA-binding and/or disordered domain-containing proteins and they associate with other cytoplasmic MLOs. FG-Nups can undergo LLPS creating three dimensional networks with hydrogel-like properties that mimic the permeability requirements of the NPC[66,48,67,68]. MX2

assembles FG-Nups at the outer face of the condensates, creating a gel-like subcompartment, that allows dynamic interactions with importins-beta.

Mutant analysis showed that phase separation of MX2 is controlled by its N-terminal 90 amino acids and by MX2 dimerization. GTP-binding and -hydrolysis, however, are dispensable but affect MX2 condensate properties. Additionally, MX2 localization at the outer face of the NPCs depends, to some extent, on its LLPS properties besides an intact NLS. Further supporting our findings that NTD controls the phase separation properties of MX2, are experiments where the first 90 amino acids of MX2 were transferred to MX1 or irrelevant dimerization competent proteins, transferring the ability to restrict HIV-1[4,26,55] and HSV-1[9] while some studies also reported cytoplasmic MX2 NTD-driven puncta formation[26,69,70].

Our data support that the ability of MX2 to phase separate and form antiviral competent condensates is regulated by a fine-tuned balance between MX2's structural characteristics and interacting proteins. Cellular factors such as TNPO1 and SAMD4A, which regulate condensate formation, impact MX2's anti-HIV-1 and HSV-1 activities, while cellular factors with varying levels of involvement between the two activities (e.g. NUP35 and NUP62), only alter the composition of the condensates, influencing the MX2 mechanism possibly by facilitating viral antigen-MX2 binding. We showed that TNPO1-MX2 binding is controlled by the first 25 amino acids, in line with Dick et al,[35] but additionally requires at least the presence of the second prion-like phase separation promoting region. Reduced nuclear membrane localization of MX2 in TNPO1-depleted cells indicates that its NPC association is also controlled by phase separation. TNPO1 is a regulator of phase separation properties by acting as a chaperone for its interacting proteins. It has been proposed that the affinity of the NLS for TNPO1 may be modulated by post-translational modifications (PTMs) occurring in or near the NLS[71–74]. Phosphorylation, can either enhance or inhibit phase separation and recently emerged as a bidirectional modulator of MX2 anti-HIV-1 activity, also controlling MX2 binding to TNPO1[36,75–77].

MX2 hinders nuclear entry of the HIV-1 and herpesvirus genome by interacting with incoming viral capsids. MX2 binds to the HIV-1 core preventing the virus uncoating process, facilitated by the NTD and GTPase domain and does not require GTP-binding and -hydrolysis[12,20,78,79]. More recently, it has been demonstrated that MX2-containing cell fractions can disassemble alphaherpesvirus capsids[8]. This process requires MX2 binding to HSV-1 capsids, GTPase activity and involves, to some extent, the first 25 residues of MX2[8,9]. Our antiviral and confocal imaging data demonstrate that only MX2 mutants that can form condensates were able to restrict HIV-1 and HSV-1, strongly suggesting an important role of LLPS in the MX2 antiviral

mechanism in addition to capsid binding and/or disassembly. The discovery of LLPS as an essential feature of the MX2 antiviral mechanism, can explain why the MX2(26-715) short isoform, that maintains partial HSV-1 and HIV-1 capsid binding and disassembly activity in cell lysates but cannot form condensates, fails to restrict either virus in a cellular context[8,9,11,78]. Moreover, underlining the indispensable role of both capsid binding and phase separation, the GTP-binding-defective MX2(K131A), which was shown to maintain binding to HIV-1 but not HSV-1 capsids, restricts only HIV-1 through its capability to generate cytoplasmic condensates[8,9,80].

Incoming HIV-1 and HSV-1 capsids colocalized with MX2 condensates. High resolution imaging, however, revealed a striking difference: HIV-1 capsids resided inside the MX2 condensates, while HSV-1 capsids were positioned at the boundary of the MX2 condensates (Fig. 6a-d). These distinct MX2 condensate-viral capsid interaction patterns remarkably resemble how HIV-1 and HSV-1, in the absence of MX2, interact with the NPC upon nuclear entry[57,58] (Fig.6a-e). Therefore, MX2-capsid binding is sufficient for the encapsulated viral genome of HIV-1 to enter the condensates, whereas the DNA genome of HSV-1 remains protected within the capsid outside of the condensates. This emphasizes the necessity for MX2 to disassemble and release the HSV-1 viral genomes to exert its anti-HSV-1 activity.

Based on (1) the MX2 condensate-viral capsids colocalization pattern, (2) the different virus-specific Nups requirements for MX2 antiviral activity, (3) the essential condensate-forming requirement of MX2's anti-HIV-1 and -HSV-1 activity, and (4) the FG-Nups assembly at MX2 condensates, we propose that MX2 condensates mimic the NPC environment, therefore acting as nuclear pore decoys that facilitate MX2-capsid association. In case of HSV-1, after disassembly and genome release by MX2, punched or flattened empty capsids could be released in the cytoplasm justifying our observations of ''delayed'' capsids that no longer interacted with MX2 in the cytoplasm of infected MX2-expressing HeLa cells.

Our nuclear pore-mimicking condensate model for MX2 can explain how Nups that localise at different sites of the NPC and can bind viral components, can affect MX2's antiviral activity. These data are not in line with the canonical view that MX2 primarily localizes at the cytoplasmic face of the NPC only interacting with NPC cytoplasmic filaments and outer-ring Nups, but support a model of a previously overlooked LLPS-driven cellular compartment in which all these diversely localized Nups could associate with MX2 to facilitate its antiviral activity. Furthermore, HIV-1 capsid mutants that are partially or completely insensitive to MX2 restriction, while still capable of interacting with MX2, have a lower nuclear entry efficiency

with altered dependence on cofactors associated with nuclear entry, and are specifically insensitive to FG-rich NUP358(RANBP2) and NUP153 depletion[6,20,43,55,56,81–84].

Both HIV-1 and HSV-1 travel along the MT network towards the centrosome and then dock to the NPC via nuclear transport factors[42,56]. Depolymerization of the MT network reduced the ability of MX2 to restrict HIV-1 but not HSV-1, suggesting that MX2 blocks HIV-1 during capsid MT-directed transport which is not the case for HSV-1. These observations correlate with the fact that HIV-1 capsids are exposed during MT-traveling allowing MX2 binding, in contrast with the HSV-1 capsids that require tegument proteins for MT motor binding[42,56]. In line with this, tegument proteins protect HSV-1 capsids against MX2 attack[8]. Additionally, MX2 inhibits herpesviruses, acting after virus entry and tegument protein dissociation but before viral DNA uncoating and nuclear import, suggesting a cytoplasmic gatekeeper role of MX2 condensates prior to capsid docking to the NPC[11]. The ability of MX2 to relocalize importins-beta to the cytoplasmic condensates via the 25 NTD amino acids could be the facilitator of MX2-HSV-1 capsid binding and subsequent disassembly.

In conclusion, by combining proteomics data, antiviral experiments, and extensive bio-imaging, we demonstrate that LLPS is an essential process in MX2-mediated restriction of HIV-1 and HSV-1. Additionally, we describe the composition and properties of MX2 cytoplasmic biomolecular condensates, which was a long-lasting missing piece of the MX2 biology. Our findings support a decoy model in which NPC-like cytoplasmic MX2-containing condensates interact with incoming HIV-1 and HSV-1 capsids diverting them away from the NPC for MX2 to trap and stabilize or disassemble them, respectively, thus preventing the nuclear entry of their viral genome.

Methods

Molecular Cloning

All the plasmids used in this study were generated by an in-house BsaI-based Golden Gate assembly cloning system. To acquire coding DNA sequence(s) [CDS(s)], complementary DNA (cDNA) derived from U87-MG was amplified by PCR. Alternatively, CDS(s) were obtained as DNA fragments from Twist Biosciences. The resulted sequences of the genes of interest (GOI) were compared with the NCBI available sequences and used if there was a 100% amino acid similarity (Sequence information can be found in Supplementary Table.4). Generation of lentiviral vectors was achieved by a Gateway cloning step following the initial Golden Gate assembly reaction to combine two expression cassettes in a lentiviral backbone. The second cassette expresses a selection marker conferring antibiotic resistance for positive selection. Required sequence mutations, for the removal of BsaI sites in CDSs or for the generation of MX2 mutants were performed by fusion PCR.

Cells

HEK293T cells originate from[85], HeLaP4 cells[86], which express the CD4 receptor, were acquired through the National Institutes of Health (NIH) AIDS reagent program, U87-MG (#HTB-14), HeLa (#CCL-2), and Vero (#CCL-81) cells were obtained from the American Type Culture Collection (ATCC). All cell lines were cultured in Dulbecco's modified Eagle medium (DMEM) GlutaMAX supplement (#10566016, Thermo Fisher Scientific), supplemented with 10% fetal bovine serum (FBS, #10270106, Thermo Fisher Scientific), 100 U ml^{-1} penicillin and 100 µg ml^{-1} streptomycin. For some experiments, culture medium was supplemented with recombinant human interferon-alpha 2 alpha (rhIFN-a2a) (#11343504, ImmunoTools), doxycycline (#D9891, Sigma-Aldrich), nocodazole (#M1404, Sigma-Aldrich), biotin (#B4639, Sigma-Aldrich), sodium arsenite ($NaAsO_2$) (#S7400, Sigma-Aldrich), polybrene infection reagent (#TR-1003-G, Sigma-Aldrich) or cycloheximide (#C4859, Sigma-Aldrich). Cells were transduced at MOI of 1 for stable introduction of transgenes. For the generation of stable doxycycline-inducible U87-MG (rtTA/tTS _MX2_MX2-T2A-TurboID) and U87-MG (rtTA/tTS _MX2_MX2-MUTT2A-TurboID) cell lines, U87-MG cells were first transduced with Tet-On transactivator (rtTA/tTS, VectorBuilder) lentivirus and selected with 200 µg ml^{-1} hygromycin (#ant-hg-1, Thermo Fisher Scientific) for 14 days. U87-MG (rtTA/tTS) were subsequently transduced with untagged MX2 expression vectors and selected with 5 µg ml^{-1} blasticidin (#ant-bl-1, Thermo Fisher Scientific) for 14 days. The final U87-MG cell lines used for the BioID experiments were

obtained by transducing the U87-MG (rtTA/tTS _MX2) cells with either MX2-T2A-TurboID or MX2-MUTT2A-TurboID lentivirus and selecting with 2 µg ml^{-1} puromycin (#ant-pr-1, Thermo Fisher Scientific) for 7 days. For the generation of stable doxycycline inducible HeLa-MX2 cell lines, HeLa cells were first transduced with rtTA/tTS lentivirus, selected and maintained with 200 µg/ml hygromycin for 14 days, similar to U87-MG. HeLa (rtTA/tTS) were then transduced with untagged MX2(1-715), V5- or EGFP-tagged MX2(1-715) or MX2 mutants and selected with 2 µg ml^{-1} puromycin.

Lentiviral vector production

Lentiviral vector stocks were obtained by transfection of 6.5 x 10^6 HEK293T cells with packaging vector gag-pol-rev (pCMV-dR8.74, #22036, Addgene), a vesicular stomatitis virus G (VSV-G) envelope expression vector (pMD2.G, #12259, Addgene) and a lentiviral transfer vector containing the transgene in a ratio of 2:1:3 by calcium phosphate transfection. The culture medium was refreshed 1-4 h before transfection and 24 h after transfection. Lentiviral particles-containing supernatants were harvested 48 and 72 h post-transfection, filtered with a 0.45 µm cutoff filter (Millex® filter, #SLHVM33RS, Millipore), concentrated by ultracentrifugation at 22.000 rpm for 2.5 h at 4°C (Optima™ XPN-80 – Beckman Coulter), redissolved in 100 µL of DMEM and stored in small aliquots at −80 °C. For HIV-1-GFP stocks intended for antiviral assays, pRRLsin.CMV-GFP plasmid was derived from (pRRLsin.cPPT.PGK-GFP.WPRE, #12252, Addgene) driving the expression of enhanced green fluorescent protein (EGFP) from a CMV promoter. HIV-1-GFP was titrated by infecting a defined number of HeLa cells and determine the percentage of infected GFP-positive cells 2 days post-transduction by flow cytometry (Attune™ NxT Acoustic Focusing Cytometer, Invitrogen). Single-round viral particles containing fluorescently labelled integrase (IN), referred to as HIV IN-EGFP, were generated by Vpr-mediated trans-incorporation as described previously[87,88]. Briefly, producer cells (HEK293T) were co-transfected with three plasmids: pVSV-G for the envelope, the HIV-1 clone pNL4-3.Luc.R^-E^- and pVpr-IN-EGFP. The viral molecular clone pNL4-3.Luc.R^-E^- was obtained through the NIH AIDS Research and Reagent Reference program[89]. Upon maturation, the HIV protease cleavage leads to the production of fluorescent IN-EGFP that is incorporated in the viral particle. Viruses were harvested 48 hours after transfection, filtered and concentrated as described above.

HSV-1 Viruses

All herpes simplex virus-1 (HSV-1) viruses used in this study were grown and titrated on Vero cells as described by Grosche et al[90]. HSV-1 strain F was kindly provided by Dr. Herman

Favoreel (Ghent University, Ghent, Belgium). The previously described[91] HSV-1 C12 recombinant HSV-1 strain SC16 containing EGFP expression cassette in the US5 locus was kindly provided by Dr. Stacey Efstathiou (University of Cambridge, Cambridge, UK). Herpes Simplex Virus-1 (HSV-1) strain 17$^+$ Lox-BAC-pHCMV-FireFly Luciferase reporter virus[92] and (HSV-1) strain 17$^+$ Lox -wild-type BAC[93] were generously provided by Dr. Beate Sodeik (Hannover Medical School, Hannover, Germany). HSV-1 strain 17$^+$ Lox -wild-type BAC[93] stocks for intracellular viral capsid microscopy experiments were gradient-purified to remove residual cell debris and cytokines as described by Grosche et al[90] using Ficoll® 400 (#F4375, Sigma-Aldrich) gradient solution.

Antibodies

The following primary antibodies were used for immunoblotting: mouse monoclonal anti-α-tubulin (#T5168, Sigma-Aldrich, dilution 1:1,000), rabbit polyclonal anti-MX1(MxA) (#H00004599-D01P, Novus Biologicals, dilution 1:5,000), rabbit polyclonal anti-MX2 (#HPA030235, Sigma-Aldrich powered by Atlas Antibodies, dilution 1:1,000), mouse monoclonal anti-V5-tag (#R960-25, Thermo Fisher Scientific, dilution 1:5,000), rabbit polyclonal anti-FLAG-tag (#F7425, Sigma-Aldrich, dilution 1:1,000), rabbit polyclonal anti-EGFP (#2555, Cell Signaling, dilution 1:1,000), streptavidin Alexa Fluor™ 680 conjugate (#S21378, Thermo Fisher Scientific, dilution 1:50,000). HSV-1 VP5 was immunoblotted with rabbit polyclonal anti-NC-1 antiserum[94] that was a generous gift by Dr. Gary H. Cohen and Dr. Roselyn J. Eisenberg (University of Pennsylvania, Philadelphia, USA). Aforementioned primary antibodies were revealed using goat polyclonal anti-mouse-IgG (IRDye® 800CW, Li-COR, dilution 1:5,000), goat polyclonal anti-rabbit-IgG (IRDye® 800CW, Li-COR, dilution 1:5,000), goat polyclonal anti-mouse-IgG (IRDye® 680RD, Li-COR, dilution 1:5,000), or goat polyclonal anti-rabbit-IgG (IRDye® 680RD, Li-COR, dilution 1:5,000).

The following primary antibodies were used for co-immunoprecipitation: mouse monoclonal anti-FLAG-BioM2 antibody (#F9291; Sigma-Aldrich).

The following primary antibodies were used for confocal microscopy: mouse monoclonal anti-V5-tag (#R960-25, Thermo Fisher Scientific, dilution 1:500), mouse monoclonal anti-α-tubulin (#MA1-19162, Thermo Fisher Scientific, dilution 1:150), mouse monoclonal anti-Human Immunodeficiency Virus Type 1 (HIV-1) p24 clone [*39/5.4A]* (#ab9071, Abcam, dilution 1:500). Mouse monoclonal anti-Human Immunodeficiency Virus Type 1 (HIV-1) p24 clone [*AG3.0]* (#ARP-4121, dilution 1:250) was obtained through the NIH HIV Reagent Program, Division of AIDS, NIAID, NIH contributed by Dr. Marie-Claire Gauduin and provided to us by Dr. Linos Vandekerckhove (Ghent University, Ghent, Belgium), and polyclonal rabbit serum directed

against HSV-1 capsids (SY4563, anti-capsid, dilution 1:500)[8,95] that was kindly provided by Dr. Beate Sodeik (Hannover Medical School, Hannover, Germany). The following secondary antibodies were used: donkey anti-mouse DyLight™ 650 (# SA5-10169, Thermo Fisher Scientific, dilution 1:1,000), donkey anti-rabbit Alexa Fluor™ 568 (#A10042, Thermo Fisher Scientific, dilution 1:500), donkey anti-rabbit Alexa Fluor™ 488 (#A-21206, Thermo Fisher Scientific, dilution 1:500), donkey anti-mouse Alexa Fluor™ 568 (#A10037, Thermo Fisher Scientific, dilution 1:500) and donkey anti-mouse DyLight™ 488 (#SA5-10166, Thermo Fisher Scientific, dilution 1:1,000).

MX2 Proximity Biotinylation (BioID) for LC-MS/MS

MX2 BioID experiments were performed in three conditions: (i) doxycycline-treated (-IFN), (ii) doxycycline-treated combined with IFNa2a stimulation (+IFN), and (iii) doxycycline-treated and infected with HSV-1 (HSV-1). All three BioID experiments were performed simultaneously using same passage U87-MG (rtTA/tTS_MX2_MX2-T2A-TurboID) and U87-MG (rtTA/tTS _MX2_MX2-MUTT2A-TurboID) cell lines. For every condition, four control samples (T2A) and four MX2 specific samples (MUTT2A) were prepared. For every sample a 145 cm^2 culture dish (Nunc) was seeded with 5×10^6 cells. Twenty-four hours after seeding, 15 ng ml^{-1} of doxycycline was added to each sample. For the +IFN condition samples the medium was also supplemented with 1,000 IU ml^{-1} rhIFN-a2a. Twenty-four hours after doxycycline stimulation, biotin was added to a final concentration of 50 µM to every culture dish, with the HSV-1 condition samples first challenged with HSV-1 strain F at MOI of 20. The virus was first inoculated on ice at 4°C for 2 h and then samples were washed with PBS and incubated with biotin containing medium at 37°C and 5% CO_2. Biotinylation was performed for 2 h for all the samples. Then the growth medium was aspirated and cells were washed two times with ice-cold PBS before were lysed in 750 µL RIPA lysis buffer (50 mM Tris-HCl pH 7.5, 150 mM NaCl, 1% NP-40, 1 mM EDTA, 1 mM EGTA, 0.1% SDS, 1X EDTA-free protease inhibitor cocktail [#04693132001, Roche], and 0.5% sodium deoxycholate) and collected using a cell scraper. Lysates were incubated with agitation for 1 h at 4 °C with 250 IU of benzonase (#70746, Millipore) followed by 15 min centrifugation at 15,000 x g at 4°C to remove the insoluble fraction of the lysate. Supernatants were transferred to a new tube and total protein concentration was determined by the Bradford protein assay to normalize input material to the maximum shared total protein amount across the samples between all three conditions. For every sample, 30 µL of streptavidin Sepharose high-performance bead suspension (#GE17-5113-01, Cytiva) was used for the enrichment of biotinylated proteins. Beads were pelleted by centrifugation at 500 x g for 1 min and washed three times in RIPA lysis buffer prior to

addition to the lysate. Affinity purification was performed on a rotator at 4°C for 3 h. Beads were recovered by centrifugation of the samples at 500 x g for 1 min at 4°C and aspirating the supernatant. Beads were washed three times in RIPA lysis buffer, twice in 50 mM ammonium bicarbonate pH 8.0, and once in 20 mM Tris-HCl pH 8.0, 2 mM CaCl2 prior to resuspension in 20 µL of 20 mM Tris-HCl pH 8.0. Trypsin digest was allowed overnight at 37°C by the addition of 1 µg of trypsin (#V5111, Promega) to each sample. Peptide mixtures were depleted of beads by centrifugation at 500 x g for 1 min, after which the supernatant was transferred to a new Eppendorf tube. To ensure complete digestion, peptide mixtures were incubated with an additional 500 ng of trypsin for 3 h before acidification with formic acid to a final concentration of 2%, followed by centrifugation at 15,000 x g at room temperature (RT). Peptides containing supernatants were transferred in mass spectrometry vials (#9301-0978, Agilent).

LC-MS/MS

Purified peptides were re-dissolved in 21.5 µL solvent A of which 2.5 µL was injected for LC-MS/MS analysis on an Ultimate 3000 RSLCnano system (Thermo Fisher Scientific) in line connected to a Q Exactive HF Biopharma mass spectrometer (Thermo Fisher Scientific) equipped with a pneu-Nimbus dual ion source (Phoenix S&T). Trapping was performed at 10 µL/min for 4 in loading solvent A on a 20 mm trapping column (made in-house, 100 µm inner diameter (ID), 5 µm beads, C18 Reprosil-HD, Dr. Maisch). The peptides were separated on a 250 mm nanoEase column (M/Z HSS T3 column, 100 Å, 1.8 µm, 75 µm I.D., Waters) kept at a constant temperature of 40°C. Peptides were eluted by a non-linear increase from 1 to 55% MS solvent B (0.1% FA in water/ACN (2:8, v/v)) over 75 min, at a flow rate of 300 nL/min, followed by a 15 min wash reaching 97% MS solvent B and re-equilibration with 99% MS solvent A (0.1% FA in water). The mass spectrometer was operated in data-dependent mode, automatically switching between MS and MS/MS acquisition for the 12 most abundant ion peaks per MS spectrum. Full-scan MS spectra (375-1,500 m/z) were acquired at a resolution of 60,000 in the Orbitrap analyzer after accumulation to a target value of 3,000,000. The 12 most intense ions above a threshold value of 13,000 (minimum AGC of 1,000) were isolated for fragmentation at a normalized collision energy of 30%. The C-trap was filled at a target value of 100,000 for maximum 80 ms and the MS/MS spectra (200-2,000 m/z) were acquired at a resolution of 15,000 in the Orbitrap analyzer with a fixed first mass of 145 m/z. Only peptides with charge states ranging from +2 to +6 were included for fragmentation and the dynamic exclusion was set to 12 sec.

Mass Spectrometry Data Processing and Analysis

Data analysis of the Obtained Xcalibur raw files (.raw) was performed using MaxQuant (version 1.6.11.0) using the Andromeda search engine with default search settings. PSM, protein, and site false discovery rates were set at 0.01. Spectra were searched against all human proteins in the Uniprot/Swiss-Prot database (database release version of January 2019 containing 20,413 protein sequences) (taxonomy ID 9606) and human herpesvirus 1 (strain 17) viral proteins taxonomy (HHV-1) (Human herpes simplex virus 1) (proteome ID UP000009294), including FASTA file for the N-terminally V5 tagged TurboID sequence. Enzyme specificity was set as C-terminal to arginine and lysine (trypsin), also allowing cleavage at arginine/lysine-proline bonds with a maximum of two missed cleavages. Methionine oxidation and N-terminal acetylation were set as variable modifications. Matching between runs was enabled with an alignment time window of 20 min and a matching time window of 0,7 min. Only proteins with at least one peptide were retained to compile a list of identified proteins. Proteins were quantified by the MaxLFQ algorithm integrated in the MaxQuant software. A minimum of two ratio counts from at least one unique peptide was required for quantification and the Fast LFQ option was disabled. The minimum peptide length was set at seven amino acids, and a maximum peptide mass of 4,600 Da was used.

Further data analysis was performed with the Perseus software (version 2.0.3.1). For each MX2 BioID condition, LFQ intensities of four control samples (T2A) and four MX2 specific samples (MUTT2A) were imported as initial matrix with the exemption of +IFN control samples (three samples). Hits identified in the reverse database, only identified by modification site and contaminants were removed and protein LFQ intensities were log2 transformed. Replicate samples were grouped, proteins with less than four valid values in at least one group were removed and missing values were imputed from a normal distribution with a width of 0.3 and a down shift of 1.8 to compile a list of quantified proteins. 2318 proteins were quantified. On the quantified proteins, for each condition a t-test was performed for a pairwise comparison between the control (T2A) and MX2 specific (MUTT2A) samples to reveal specific MX2 interaction partners. Number of randomizations was set to 1,000, FDR to 0.01 and S0 to 1. The results of these t-tests are shown in the volcano plots in Fig. 1 visualized using RStudio also showing proteins identified with an FDR 0.05. For each differential analysis, the log2 (T2A/MUTT2A) fold change value is indicated on the X-axis, while the statistical significance (−log10 p-value) is indicated on the Y-axis. Proteins outside the curved lines, set by an FDR value of 0.01 or 0.05 and an S0 value of 1, represent specific MX2 interaction partners.

<u>MX2 SAFE network</u>

The MX2 SAFE network was generated by the FDR 0.01 enriched common MX2 interactors between the three MX2 BioID conditions (-IFN, +IFN, HSV-1). Using Cytoscape[96] (version 3.6.1), the complete BioGRID Protein-Protein Interactions network (*H. sapiens*) was uploaded and the 230 commonly enriched proteins were used to filter the nodes and edges to build the MX2 network as edge-weighted spring-embedded layout. SAFE[97] is an automated network annotation tool that requires annotations for network nodes. Using g:Profiler[98] we created an attribute file list of all known GO (Gene Ontology) cellular component terms assigned to each node of the MX2 network that we coupled to SAFE reaching 98% network coverage. SAFE analysis was performed assuming edges of the network are undirected, map-weighted distance, with 15 percentile threshold (manual assessment suggested that a value in this range should be suitable). SAFE generates an enrichment score for each node according to evidence of association to a specific GO cellular component term and assigns a color according to that score generating separate clusters ("domains" or ''landscapes'' in SAFE terminology) with a known GO term. To build a composite map, a minimum of 5 nodes was set as minimum landscape size. The final MX2 SAFE network was generated by visualizing the 4 main (umbrella) landscapes resulted from the analysis and export the resulting SAFE network as PNG image.

Protein network visualization and Dotplot generation

Following SAFE analysis in Cytoscape, nodes and edges clustering to individual SAFE domains of the MX2 SAFE network were selected and visualized as separate protein networks maintaining the same layout. The color of the nodes for each protein network was selected according to the SAFE assigned GO-specific color. For the nuclear pore protein network the nodes layout was manually organized at specific protein sub-clusters and subcomplexes according the NCP organization described by[99].

For the proteins of each network, dotplot analysis was generated using RStudio with the size and color of each dot representing the protein enrichment (log2(FC)) and statistical significance (−log10 p-value), respectively. Proteins are ranked according to their average enrichment (log2(FC)) in all three BioID conditions.

SDS-PAGE and immunoblotting

Cells were lysed in 2X Laëmmli buffer (125 mM Tris-HCl pH 6.8, 4% SDS, 20% glycerol, 0.004% Bromophenol blue supplemented with 20 mM dithiothreitol [DTT]), in TAP lysis buffer[41] (50 mM HEPES-KOH [pH 8.0], 100 mM KCl, 2 mM EDTA, 0.1% NP-40, 10% glycerol) or in RIPA lysis buffer (50 mM Tris-HCl pH 7.5, 150 mM NaCl, 1% NP-40, 1 mM EDTA, 1 mM EGTA, 0.1%

SDS) both supplemented with 1X EDTA-free protease inhibitor cocktail (#04693132001, Roche). For the two latter lysis conditions lysates were complemented with XT sample buffer (#1610791, Bio-Rad) and XT reducing agent (#1610792, Bio-Rad) to a final volume of 30 µL. Protein samples were boiled for 10 min at 95 °C prior to SDS-PAGE. Samples were loaded on 4–20% polyacrylamide gradient gels (#M42015, GenScript), according to the guidelines of the manufacturer. Proteins were transferred to PVDF membrane (#IPFL00010, Merck) for 3 h at 60 V or for 30 minutes at 100 V in blotting buffer (48 mM Tris, 39 mM glycine, 0.0375 % SDS and 20 % methanol). Membranes were blocked for 1 h at room temperature (RT) with blocking buffer (#927-50000, LI-COR) and incubated with primary antibodies overnight at 4°C in blocking buffer. The next day, membranes were washed four times for 10 min with TBS-Tween20 0.1% (v/v) buffer (TBS-T) and further incubated at RT for 1 h with the appropriate secondary antibody in blocking buffer. Membranes were washed four times for 10 min with TBS-T. Immunoreactive bands were visualized on a LI-COR-Odyssey infrared scanner (Li-COR).

Co-immunoprecipitation

Coimmunoprecipitations were performed to confirm the interaction between MX2-TurboID fusion protein with FLAG-tagged MX2. Eight million HEK293T cells were seeded in 10-cm tissue culture dish. The following day, cells were transfected using polyethylenimine (PEI) (#23966-1; Polysciences, Inc.) with 5 µg of the indicated DNA constructs using a 1:5 ratio with PEI. Twenty-four hours after transfection, cells were lysed with TAP lysis buffer supplemented with 1 mM dithiothreitol [DTT], 0.5 mM phenylmethylsulfonyl fluoride (PMSF), 0.25 mM sodium orthovanadate, 50 mM B-glycerophosphate, 10 mM NaF, and 1X EDTA-free protease inhibitor cocktail. Lysates were incubated with 1 µg anti-FLAG-BioM2 antibody (#F9291, Sigma-Aldrich) or without antibody for 3 h at 4°C under constant rotation. Afterwards protein complexes were immunoprecipitated by the addition of 10 µL of magnetic Dynabeads™ MyOne™ Streptavidin T1 (#65601, Thermo Fisher Scientific) for 10 min at RT under constant rotation. Beads were captured in magnet and washed 2 times with lysis buffer followed by protein elution directly in 1X loading buffer. Proteins that bound to the beads were detected by immunoblotting.

DNA plasmid transfection

Plasmid transfection for overexpression of untagged MX2 and MX2-T2A or MUTT2A-TurboID expression vectors, 1 million HEK293T cells were seeded into 6-well plates and transfected using polyethylenimine (PEI) (#23966-1; Polysciences, Inc.) with 1 µg of the indicated DNA constructs at a 1:5 ratio with PEI. For HSV-1 C12 strain transient expression antiviral

experiments, 10,000 HeLa cells were seeded into 96-well black/clear bottom plates and transfected using PEI with 70 ng of the indicated DNA constructs at a 1:5 ratio with PEI. For transient expression microscopy experiments, 15,000 HeLa based cells were seeded into 8-well imaging µ-Slide (#80826, Ibidi GmbH) and transfected using FUGENE HD (#E2311, Promega) with 100 ng of DNA at 1:3 ratio with FUGENE HD.

siRNA-mediated knockdown

For the RNA interference (RNAi) based imaging and functional experiments using HSV-1 firefly and HIV-1-GFP reporter viruses, 15,000 HeLa based cells were seeded in 48-well plates and transfected, with 15 nM (single gene target) or 30 nM (two gene targets or single gene target with Non-Targeting siRNA, 15 nM each) of SMARTpool siRNAs (Dharmacon) (siRNA gene specific catalog numbers can be found in Supplementary Table.4) according to manufacturer's instructions using DharmaFECT 1 transfection reagent (#T-2001-02, Horizon) in antibiotic free medium. Six hours post-transfection the medium was refreshed with complete culture medium. For the RNA interference (RNAi) based functional experiments using HSV-1 C12 strain GFP reporter virus, 5,000 HeLa based cells were seeded in 96-well black/clear bottom plates and transfected as described above.

RT-qPCR for siRNA-mediated knockdown efficiency validation

cDNA synthesis was performed using the PrimeScript RT kit (#RR037A, Takara Bio) using 250 ng RNA input from siRNA transfected HeLa MX2 cells, collected 24 h after transfection. TNPO1, TNPO2, SAMD4A, SAMD4B, NUP58, NUP62, NUP35, NUP54, TRIM26, TRIM56, FUBP3, and FAM120C specific primer pairs were designed using the PrimerQuest design tool (IDT, primers list can be found in Supplementary Table.4). Target transcripts were amplified with the SensiFAST SYBR No-ROX kit (#BIO-98005, Meridian Bioscience) according to the manufacturer's instructions and signal was detected using a LightCycler 480 System (Roche). Samples were measured in technical duplicates in a 384-well plate. The following cycling conditions were used: 1 cycle at 95°C for 5 min, 40 cycles at 95°C for 10 s, 60°C for 10 sec and 72°C for 10 sec, followed by melting curve analysis to validate unique amplicons. Quantitation cycles (Cq) were normalized to housekeeping genes (SDHA, UBC, YWHAZ) using geometric averaging. Normalized Cq values were subsequently normalized relative to the Non-Targeting siRNA sample. All RT-qPCR analyses were done in qbase+ (CellCarta), the geNorm algorithm was used to ensure stability of the housekeeping genes across all samples[100]. Visualization of the data was performed in GraphPad Prism.

In vitro infection with Herpes Simplex Virus Type 1 strain C12 GFP reporter virus (HSV-1 C12)

Twenty-four hours after siRNA/DNA transfection or doxycycline stimulation of HeLa-derived cells, seeded in 96-well black/clear bottom plates, cells were challenged with HSV-1 C12 at MOI of 0.05. Infection was maintained in 2% FBS FluoroBrite DMEM medium (#A18967-01, Thermo Fisher Scientific), supplemented with/out doxycycline when doxycycline-inducible HeLa MX2 or HeLa MX2(1-715) and mutants V5 tagged were used. GFP fluorescence was monitored at 24 h intervals using the Infinite® 200 PRO Reader and Tecan iControl Software (Tecan Life Sciences). Each individual measurement (n = 4) was normalized to the mean value of the uninfected wells (n = 4). The relative area under the curve from 0 to 72 h post-infection was calculated for each growth curve. For proteins expression analysis, 48 h post-infection cells from a single well were washed with ice-cold PBS and collected in 2X Laëmmli buffer.

In vitro infection with Herpes Simplex Virus-1 (HSV-1) strain 17^{+} Lox-BAC-pHCMV-FireFly Luciferase reporter virus (HSV-1 firefly)

Forty-eight hours after siRNA transfection or doxycycline stimulation of HeLa-derived cells, seeded in 48-well plates, cells were challenged with HSV-1 firefly reporter virus at MOI of 1. Infection was maintained in 2% FBS DMEM medium supplemented with/out doxycycline. Six and a half hours post-infection cells were lysed in 50 µL of 1X Passive Lysis Buffer and luminescence was determined using the Luciferase Assay Substrate of the Dual-Luciferase® Reporter Assay System (# E1910, Promega), measured on a plate reader (GloMax® Navigator Microplate Luminometer, Promega). For proteins expression analysis, the same lysates were used.

In vitro infection with HIV-1 based lentiviral vector expressing EGFP (HIV-1-GFP)

Forty-eight hours after siRNA transfection or doxycycline stimulation of HeLa-derived cells, seeded in 48-well plates, cells were challenged with HIV-1-GFP reporter virus. Infection was maintained in 10% FBS DMEM supplemented with 8 µg ml^{-1} polybrene infection reagent (#TR-1003-G, Sigma-Aldrich). Twenty-four hours post-infection cells were washed with PBS and the medium was refreshed with complete culture medium. The percentage of infected GFP-positive cells was determined 48 h post-transduction by flow cytometry (Attune™ NxT Acoustic Focusing Cytometer, Invitrogen), following cell detachment and fixation with 4% paraformaldehyde (PFA).

Analysis of HSV-1 capsids intracellular localization

HeLa-derived cells were inoculated with gradient purified HSV-1 strain 17+ Lox -wild-type BAC virus stock (MOI:50) in RPMI 1640 medium, GlutaMAX™ supplement (#61870010, Thermo Fisher Scientific) containing 0.2% (w/v) Bovine Serum Albumin (BSA) and 20 mM HEPES for 2 h on ice to allow virus binding. After 2 h, cells were washed twice with RPMI 1640 medium, and incubated for 2.5 h at 37°C and 5% CO_2 in 2% FBS DMEM supplemented with 100 µg ml^{-1} cycloheximide (#C4859, Sigma-Aldrich) to prevent viral proteins synthesis. Subsequently, HSV-1 infected cells were fixed using 3% paraformaldehyde (PFA) in PBS for 10 min at RT and then permeabilized with 0.2% Triton X-100 in PBS for 10 min at RT. Detection of intracellular incoming capsids was achieved by staining the infected cells with pre-absorbed anti-capsids SY4563 antibody. Briefly, SY4563 antibody was diluted 1:100 in blocking buffer and pre-absorbed with fixed and permeabilized HeLa cells in a 6-well plate with constant rocking overnight (O/N) at 4°C. The next day, the pre-absorbed antibody was collected in an Eppendorf tube and centrifuged for 5 min at 15,000 x g at RT. Antibody containing supernatant was collected and diluted in a final volume of 1:500 in blocking buffer.

Analysis of HIV-1 capsids intracellular localization

HeLa-derived cells were inoculated with filtered (0.45 µm, 33 mm Millex® filter, #SLHVM33RS, Millipore) lentiviral particles (MOI:25) for 1 h on ice in culture medium in the presence of 100 µg ml^{-1} cycloheximide and 8 µg ml^{-1} polybrene infection reagent (#TR-1003-G, Sigma-Aldrich) and then placed at at 37°C and 5% CO_2. After 6 h, cells were fixed using 3% paraformaldehyde (PFA) in PBS for 10 min at RT and then permeabilized with 0.2% Triton X-100 in PBS for 10 min at RT. Detection of intracellular incoming capsids was achieved by staining the infected cells with mouse monoclonal anti (HIV-1) p24 clone [39/5.4A] or clone [AG3.0] antibodies.

Analysis of HIV IN-EGFP particles intracellular localization

One day prior to infection, 30,000 HeLaP4 cells were seeded into 8-well imaging µ-Slide (#80826, Ibidi GmbH) that was previously coated with 0.1 mg ml^{-1} Poly-D-lysine hydrobromide (#P6407, Sigma-Aldrich). The following day, cells were transfected with MX2-mScarlet vector using FuGENE 6 transfection reagent (#E2691, Promega) following the manufacturers protocol. The cells were maintained in 10% FBS DMEM at 37°C and 5% CO_2. After 24 hours, when the MX2-mScarlet protein was expressed, the cells were infected with IN-EGFP VSV-G pseudotyped HIV-1 virus (HIV IN-EGFP) with an amount corresponding to 4 µg of p24 antigen. After 6 hours, the cells were washed with PBS and fixed in 4% paraformaldehyde (PFA) in PBS for 15 min at RT. After fixation, the cells were treated with 1 µg ml^{-1} nuclear stain NucSpot

650/665 (#41034, Biotium) for 30 min at RT. The cells were washed again and stored in PBS at 4°C until imaging.

Nocodazole treatment

For antiviral assays, 15,000 HeLa MX2 cells were grown with/out doxycycline in 48-well plates. Twenty-four hours after stimulation medium was refreshed with DMSO or 1, 5 or 10 µM of nocodazole supplemented culture medium. Three hours after nocodazole treatment cells were infected in the presence similar DMSO or 1, 5 or 10 µM of nocodazole conditions. For HSV-1 firefly reported virus challenge, the infection was maintained in DMSO or 1, 5 or 10 µM nocodazole supplemented 2% FBS DMEM medium for 6,5 h followed by cell lysis. Luminescence was determined as described before. For HIV-1-GFP challenge, the infection was maintained in DMSO or 1, 5 or 10 µM nocodazole supplemented 10% FBS DMEM medium with 8 µg mL^{-1} polybrene infection reagent (#TR-1003-G, Sigma-Aldrich). Seven hours after transduction, cells were washed with PBS and the medium was refreshed with 10% FBS DMEM medium. The percentage of infected GFP-positive cells was determined 48 h post-transduction by flow cytometry as described before.

For MX2-EGFP/tubulin confocal microscopy, 15,000 HeLa cells were seed into 8-well imaging µ-Slide (#80826, Ibidi GmbH) and transfected with MX2(1-715)-EGFP expression vector. Twenty-four hours after transfection, medium was refreshed with DMSO or 1, 5 or 10 µM of nocodazole supplemented culture medium. Three hours after nocodazole treatment cells were fixed using 2% paraformaldehyde (PFA) in PBS for 10 minutes at RT and permeabilized with 0.2% Triton X-100 in PBS for 10 min at RT. Detection of MTs was achieved by staining the treated cells with mouse monoclonal anti-α-tubulin antibody.

NanoBIT complementation assay

For NanoBIT experiments 12,000 HeLa cells were seeded in 96-well black plates and each well was transfected with 100 ng of total DNA using 1:3 ratio of FUGENE HD (#E2311, Promega). Different amounts of plasmid DNA were used to achieve comparable expression of LgBiT/FLAG-tagged and SmBiT/V5-tagged proteins. LgBit and SmBiT complementation generated luminescent signal was measured in live cells using Nano-Glo® Live Cell Assay System (#N2011, Promega) according to the manufacturer's instructions. In brief, 24 h after transfection cells were washed with PBS and the medium was replaced with 100 µL of FBS-free DMEM medium. Luminescence was determined by adding 25 µL of Nano-Glo® Live Cell Reagent to each well and after a 10 min incubation period, measurements were taken for 15 min, 1 measurement per min, on a plate reader (EnSight Multimode Plate Reader or EnVision

XCite 2105 Multimode Plate Reader, PerkinElmer). The final graph and heat map resulted by calculating the average of all 15 measurements for each technical replicate. For proteins expression analysis, after measurements, cells from a single well were washed with ice-cold PBS and collected in 2X Laëmmli buffer.

Confocal Microscopy

15,000 HeLa based or U87-MG cells were seeded into 8-well imaging µ-Slide (#80826, Ibidi GmbH). For transient expression experiments each well was transfected with 100 ng of DNA using 1:3 ratio of FUGENE HD (#E2311, Promega). Twenty-four hours after transfection or doxycycline stimulation, cells were fixed using, prewarmed to 37°C, 2% paraformaldehyde (PFA) in PBS for 10 min at RT. Fixed cells were washed three times for 5 min in PBS and then permeabilized with 0.2% Triton X-100 in PBS for 10 min at RT. Cells were washed with PBS followed by 1 h incubation in blocking buffer [PBS complemented with 0.5% BSA (IgG-Free, Protease-Free, #001-000-162, Jackson ImmunoResearch), 0.02% Triton X-100 and 1:100 diluted donkey serum] at RT. Cells were incubated overnight at 4°C with primary antibodies diluted in blocking buffer. The next day, cells were washed three times for 5 min in PBS and then incubated for 2 h with secondary antibodies diluted in blocking buffer. After the secondary antibody was washed three times for 5 min, nuclei were stained with DAPI (4',6-Diamidino-2-Phenylindole, Dihydrochloride) (#D1306, Thermo Fisher Scientific) (dilution 1:1,000 in PBS) for 15 minutes at RT and, after washing, cells were maintained in PBS or in polyvinyl alcohol mounting medium with DABCO (#10981, Supelco). Imaging of U87-MG cells either mock transfected or expressing MX2-T2A-TurboID or MX2-MUTT2A-TurboID (Supplementary Fig.1e) was performed on a confocal spinning disk system (Carl Zeiss, Zaventem, Belgium). All the other imaging data in this study, were collected on an LSM880 Airyscan (Carl Zeiss, Jena, Germany) with either a Plan-Apochromat 63x/1.4 Oil, DIC M27 or a Plan-Apochromat 40x/1.3 Oil DIC UV-IR M27. The operating software is ZEN Black 2.3 SP1. The lasers used to excite the different fluorophores were a 405, 561, and 633 nm diode laser, and the 488 nm line of an Argon laser. The corresponding filter sets used were BP 420-480, LP570, LP645, and BP 495-550 in conjunction with the Airyscan detector in the SuperResolution (SR) mode of the FastAiryScan or in full Airyscan. A pixel reassignment and 2D wiener deconvolution step were carried out post-acquisition in ZEN Black. Image processing was performed using the ZEN Blue 3.5 software. For quantification purposes: Z-stacks covering the whole cell volume were recorded with the optimal z-interval according to the Nyquist criterium being 0.16 µm. A pixel reassignment and 3D wiener deconvolution step were carried out post-acquisition in ZEN Black. Imaging of HIV IN-EGFP particles was done at the KU Leuven

cell and tissue imaging core using LSM880 Airyscan (Carl Zeiss, Jena, Germany) in SuperResolution (SR) mode of the FastAiryScan mode with a Plan-Apochromat 63x/1.4 Oil, DIC M27. A field of view was selected with full cell volume and IN-EGFP viral particles. Z-stacks were taken to visualize the bulk of cytoplasm and as many viral particles as possible. IN-EGFP, MX2-mScarlet and NucSpot 650/665 were excited using laser wavelengths of 488 nm, 561 and 633 nm, respectively. The corresponding emission filter sets used were BP 495-550, 495-620, and LP 645.

Live cell imaging

Cells were seeded and transfected into 8-well imaging µ-Slide (#80826, Ibidi GmbH) and maintained during the experiments in culture medium at at 37°C and 5% CO_2. Twenty-four hours after transfection live cell imaging was carried out on the LSM880 Airyscan (Carl Zeiss, Jena, Germany) with a Plan-Apochromat 63x/1.4 Oil, DIC M27. For this purpose, we used the Airyscan detector in the SR mode of the FastAiryScan. The set-up is equipped with an incubation chamber allowing CO_2 and temperature control which was set at 37°C. The focus over time was maintained making use of the definite focus 2. The cells were monitored over a period of 37 min and 45 sec (150 frames) with a time interval of 15 sec. Accelerated videos were generated in ZEN blue 3.5 using a frame rate of 8 frames/sec.

FRAP

Cells were seeded and transfected into 8-well imaging µ-Slide and maintained during the experiments in culture medium at at 37°C and 5% CO_2. Twenty-four hours after transfection, FRAP analysis was carried out on the LSM880 Airyscan (Carl Zeiss, Jena, Germany) in the regular confocal mode with a Plan-Apochromat 63x/1.4 Oil, DIC M27. The set-up is equipped with an incubation chamber allowing CO_2 and temperature control which was set at 37°C. For each condition 7-10 condensates were measured. In each measurement 3 regions of interest (ROI) were analysed: one that was bleached (R1), one non-bleached in the background (R3), and one non-bleached in the neighbourhood of the bleached ROI (R2) to correct for the bleaching effect during imaging. The bleaching step was carried out using the 488 nm line of the Argon laser (for EGFP) with 2 iterations with 100% laser power, while the 561 nm laser was used for imaging mScarlet-tagged proteins. In the imaging sequence 10 images were taken prior to bleaching and 55 after bleaching resulting in a sequence of 100-120 sec in total (indicated in figures). From these data individual frames/images from representative FRAP experiments for each condition were selected to visualise the pre-bleached and post-bleached condensates. The recovery curves were obtained by subtracting the background signal (R3)

from the data measured in the bleached region of interest (ROI) (R1). The resulting data were normalised relevant to the bleach point set as 0 and then normalized making use of the non-bleached neighbouring ROI (R2). These normalized data were fitted in a curve with nonlinear regression using one phase association model made in GraphPad Prism. From these fitted data we could extract the half-time (t1/2) and the plateau recovery for each EGFP-tagged protein component of the condensates.

Line profiles in ZEN blue 3.5

To get information on the intensity distribution of (1) MX2-V5 with NUPL1-EGFP and (2) MX2 (1-715) and mutants EGFP-tagged with IPO4-mScarlet, a line was drawn (in the profile menu) through the structures of interest. The resulting graph shows the intensity distribution of the selected channels versus the distance of the line.

Quantification in Arivis vision 4D version 4.0.0 (Carl Zeiss):

All analysis is performed based on high resolution z-stacks recorded with a system optimized z-interval using the SR mode of the FastAiryScan of the LSM880 (Carl Zeiss, Jena, Germany). Quantification of the MX2 mutants V5-tagged condensates: For this analysis 54 randomly selected cells of each MX2 mutant were measured. MX2 condensates were identified using the blob finder operation and an object feature filter which excludes the objects smaller than 0.1 μm^3 and with a roundness factor smaller then 0.7. The number of MX2 condensates per cell were determined for all the described mutants. Quantification of the MX2 condensates in different siRNA treatments: For this analysis 96 randomly selected doxycycline-induced HeLa MX2(1-715)-EGFP cells of each siRNA variant were measured. MX2 condensates were identified using the blob finder operation. To discriminate between the total and the larger condensates, an object feature filter was applied excluding all condensates smaller than 0.1 μm^3 for the total population and smaller than 2 μm^3 for the larger condensates. The number of total MX2 condensates (including large) and % of large condensates were determined per cell for all the described siRNA variants. Quantification of the number of HSV-1 capsids in the total cell volume and in the nucleus for the different MX2 mutants: For this analysis 44 randomly selected infected cells of each MX2 mutant were measured. HSV capsids were identified using the blob finder operation. The nuclei were identified using an intensity threshold segmenter operation on the DAPI signal. Making use of the compartment operation we identified the capsids within the nuclear signal. The total number of capsids and the % of nuclear capsids were determined per cell for each of the MX2 mutants.

Statistical analysis and reproducibility

Data are represented as mean ± s.d. of experimental replicates, with the exact statistical tests, significant p values and n values indicated in the figure legends. BioID experiments were performed with ≥3 biological replicates per condition. Differences between experimental groups were evaluated, either by paired or unpaired two-tailed t-tests using GraphPad Prism. Experimental data not subjected to statistical analysis (e.g. Western blots, NanoBit assay, confocal imaging, live cell imaging, virus capsids intracellular microscopy) have been reproduced in at least three independent experiments.

Data availability

The authors declare that the plasmids and cell lines used in this study are available upon reasonable request. All datasets generated in this study are disclosed as source data. Complete protein lists, plasmid sequences, primers and siRNA information are provided in supplementary tables. The mass spectrometry proteomics data have been deposited to the ProteomeXchange Consortium via the PRIDE[101] partner repository with the dataset identifier PXD042544.

Acknowledgements

We are grateful to Dr. Herman Favoreel, Dr. Stacey Efstathiou, Dr. Gary H. Cohen, Dr. Roselyn J. Eisenberg, Dr. Beate Sodeik, and Dr. Linos Vandekerckhove for the generous provision of tools including precious antibodies and virus stocks. We would like to thank Dr. Beate Sodeik, Dr. Manutea Christophe Serrero (Aarhus University, Aarhus, Denmark) and Dr. Katinka Döhner (Hannover Medical School, Hannover, Germany) for the advice and technical protocols they kindly shared with us and Dr. Jonathan Maelfait (Ghent University and VIB, Ghent, Belgium) for the helpful discussions. We acknowledge Katie Boucher from the VIB Proteomics Facility (VIB-UGent) for operating the MS instrument and Dr. Linos Vandekerckhove's team member Zoe Stylianidou for arranging the anti-(HIV-1) p24 clone [*AG3.0]* antibody delivery. G.D.M. was supported by an FWO strategic basic research PhD student fellowship. This work was also supported by FWO projects VIREOS (G0H7518N) and VIREOS 2.0 (G0H7322N) to X.S and by an FWO project grant (G042918N) to S.E.

Figure legends

Figure 1: MX2 proximal interactome reveals association of MX2 with nuclear transport proteins and cytoplasmic granule-associated ribonucleoproteins.

a, Volcano plots of the three MX2 BioID conditions (-IFN, +IFN, HSV-1) showing the results of a t-test, comparing proteins enriched in the U87-MG MX2-MUTT2A-TurboID cell line versus proteins enriched in the U87-MG MX2-T2A-TurboID cell line (n = 4 replicates). Proteins outside the FDR 0.05 (lighter colored) and FDR 0.01 (darker colored) curved lines represent specific MX2 interaction partners annotated by gene name. Proteins previously reported to associate with MX2 as interaction partners or known to functionally impact MX2 activity are indicated with normal, while novel candidate protein partners researched in this study are indicated with bold font. Bait protein MX2 is indicated in red. **b,** Left panel: Venn diagram of MX2 associated proteins (FDR 0.01) for the three BioID conditions (-IFN, +IFN, HSV-1). ISGs only identified in the +IFN condition are indicated. Right panel: SAFE visualization of the MX2 network. The commonly enriched proteins used to build the MX2 SAFE network shown as edge-weighted spring-embedded layout. Each node represents a protein in the network, colored according to a SAFE enrichment score matching evidence of association to a specific Gene Ontology (GO) cellular component term. Different clusters are visualized using different color patterns. **c,** Upper panel: Nodes and edges of the SAFE enriched ''nuclear pore'' domain, selected and visualized as a separate protein network, clustered in specific protein sub-clusters and subcomplexes. Bottom panel: Schematic diagram of the NPC according to[99], created with BioRender software. **d,** Dotplot of nuclear pore domain proteins ranked according to their average enrichment (log2(FC)) in all three conditions. **e,** Bar chart showing the top 5 InterPro analysis predicted domains for the proteins of the nuclear pore domain. **f,** Sequences of an assortment of disordered human FG-rich Nups according to UniProt, with different color-coded FG-repeat types. **g,** Dotplot of granule ribonucleoprotein domain proteins ranked according to their average enrichment (log2(FC)) in all three conditions. **h-i,** Bar chart showing the top 5 **h,** GO cellular components terms, **i,** InterPro analysis predicted domains, for the proteins of the granule ribonucleoprotein network. **J,** Venn diagram of the granule ribonucleoprotein network and the Youn *et al.*[41] PB subnetwork.

Figure 2: SAMD4A, TNPO1, and NUP35 are required for MX2-mediated antiviral activity against HIV-1 and HSV-1, whereas NUP62 is required for HIV-1 only.

a,b Doxycycline-inducible HeLa MX2 cells were transfected with 15 nM siRNA or (**c**) with combinations of 15 nM siRNA (total 30 nM) targeting individual MX2 BioID identified target

genes. After 6 h, cells were left untreated or were induced with 100 ng mL^{-1} doxycycline. **a,** Left panel: 48 h after transfection, cells were infected with HSV-1 firefly reporter virus (MOI:1). Cells were lysed 6.5 h.p.i. and luminescence was measured. Results are shown relative to the Non-Targeting (-doxy) condition. Protein expression was analysed by immunoblot using anti-MX2, and anti-tubulin antibodies. Right panel: Fold MX2-mediated HSV-1 inhibition was calculated by dividing luminescence of the untreated by the doxycycline-induced samples in each condition (mean ± s.d., n = 3 independent experiments, two-tailed unpaired *t*-test to Non-Targeting siRNA; *p* values indicated with $*p < 0.05$, $**p < 0.01$, $***p < 0.001$). **b,** Left panel: 48 h after transfection, cells were challenged with HIV-1-GFP (MOI:0.4). Transduction efficiency was assessed 48 h post-challenge by flow-cytometry. Right panel: Fold MX2-mediated HIV-1 inhibition was calculated by dividing % GFP+ cells of the untreated by the doxycycline-induced samples in each condition (mean ± s.d., n = 3 independent experiments, two-tailed unpaired *t*-test to Non-Targeting siRNA; *p* values indicated with $*p < 0.05$, $**p < 0.01$, $***p < 0.001$). **c,** Twenty-four hours after transfection, cells were infected with HSV-1 strain C12 (MOI:0.05) in the absence or presence of 10 ng mL^{-1} doxycycline. Viral growth was determined by real-time quantification of GFP signal every 24 h until 72 h.p.i. Upper panel: Data points indicate the green GFP fluorescent intensity normalized by subtracting the mean intensity of the mock-infected samples (mean ± s.d., n = 4 biological replicates). Middle panel: Relative area under the curve (AUC) from 0 h to 72 h.p.i. was calculated for each condition. AUC are relative to Non-Targeting (-doxy) samples which are each set to 1. Lower panel: Fold MX2-mediated HSV-1 inhibition was calculated by dividing AUC of the untreated by the doxycycline-induced samples in each condition (mean ± s.d., n = 4 independent experiments, two-tailed paired *t*-test to Non-Targeting siRNA; *p* values indicated with $*p < 0.05$, $**p < 0.01$, $***p < 0.001$). a.u., arbitrary units. Protein expression was analysed on lysates obtained 48 h.p.i. by immunoblot using anti-MX2, anti-tubulin, and anti-NC-1(VP5) antibodies.

Figure 3: SAMD4A, TNPO1, and NUP35 interact with MX2 at dynamic cytoplasmic biomolecular condensates.

a, HeLa cells mock-transfected or expressing V5- or EGFP-tagged MX2. Intracellular localization of MX2 was assessed 24 h post-transfection by confocal microscopy. **b,** HeLa cells mock-transfected or (co)expressing LgBiT/FLAG-tagged MX2 and SmBiT/V5-tagged MX2, LacZ, SAMD4A, TNPO1, or NUP35. Upper panel: Reconstituted luminescence measurements for all the combinations of LgBiT-, SmBiT-tagged proteins (mean ± s.d., n = 2 biological replicates).

Lower panel: Cells were lysed and proteins were analysed by immunoblot using anti-FLAG, anti-V5, and anti-tubulin antibodies. Representative experiment performed at least three times. RLU: Relative light units. **c,** HeLa cells expressing EGFP-tagged SAMD4A, TNPO1, or NUP35 in the presence or absence of MX2-V5. Intracellular localization of the EGFP- and V5-tagged proteins was assessed 24 h post-transfection by confocal microscopy. **d-e,** HeLa cells expressing **d,** MX2-EGFP or **e,** MX2-mScarlet together with EGFP-tagged SAMD4A, TNPO1, or NUP35 imaged under time-lapse conditions. Bottom "zoom" panels show an enlarged view of the highlighted white boxed areas. Moving and fusing MX2 condensates are indicated with white arrows and Smaug1 condensates with yellow arrows. Real imaging time is indicated at the bottom left side of each image. Scale bar: 10 µm. **f,** HeLa cells expressing MX2-V5 together with different combinations of EGFP- and mScarlet-tagged proteins. Intracellular localization of the MX2-V5 and EGFP- and mScarlet-tagged proteins was assessed 24 h post-transfection by confocal microscopy. **g-h,** HeLa cells expressing **g,** MX2-EGFP or **h,** MX2-EGFP together with TNPO1-mScarlet or EGFP-tagged SAMD4A, TNPO1 or NUP35 together with MX2-mScarlet. FRAP was performed for the complete individual condensates 24 h post-transfection. Left panel: Normalized FRAP curve(s) obtained for EGFP signal over time (n=10). Plateau and half-time are indicated on the right. Right panel: Representative images showing the biomolecular condensates during FRAP (before bleaching, during bleaching, and 43 and 103 sec post-bleaching). Bleached, non-bleached, and background area are highlighted with solid, dashed, or dotted white circles, respectively. Scale bar: 10 µm. In **a, c, f** Nuclei were stained with DAPI. Scale bar: 20 µm. Right "zoom" panels show an enlarged view of the highlighted white boxed area in individual fluorescence channels and channels overlay (without DAPI).

Figure 4: MX2 assembles FG-Nups and importins-beta at cytoplasmic biomolecular condensates.

a, HeLa cells mock-transfected or expressing EGFP-tagged NUPL1 or IPO4 in the presence or absence of MX2-V5. Intracellular localization of the EGFP- and V5-tagged proteins was assessed 24 h post-transfection by confocal microscopy. **b-e,** HeLa cell expressing **b,** NUPL1-EGFP and MX2-V5 from **a**. Cells were analysed by confocal microscopy with z-series image acquisition. Left panel: Image representing a single z-slice of the complete cell. Right upper panel: "zoom" panels show an enlarged view of the highlighted white boxed area in individual fluorescence channels and channels overlay, represented as 3D volume reconstruction or as a single z-slice. Right lower panel: Intensity profile graph of NUPL1 and MX2. **c,** NUPL1-V5, MX2-mScarlet and IPO4-EGFP. Intracellular localization of the V5-, mScarlet-, and EGFP-

tagged proteins was assessed 24 h post-transfection by confocal microscopy. **d,** mScarlet-tagged MX2 together with EGFP-tagged NUPL1 or IPO4 were imaged under time-lapse conditions. For MX2 and NUPL1 individual fluorescence channels, upper ''zoom'' panels show an enlarged view of the highlighted area (white dashed squares). Bottom "zoom" panels show an enlarged view of the highlighted white boxed areas. Moving and fusing MX2 condensates are indicated with white arrows. Real time of imaging is indicated at the bottom left side of each image. Scale bar: 10 µm. **e,** MX2-EGFP together with NUPL1-mScarlet or expressing EGFP-tagged NUPL1 or IPO4, together with MX2-mScarlet. FRAP was performed for the complete individual condensates 24 h post-transfection. Left panel: Normalized FRAP curves obtained for GFP signal over time (n=7). Plateau and half-time are indicated on the right of each curve. Right panel: Representative images showing the biomolecular condensates during FRAP (before bleaching, during bleaching, and 34 and 84 sec post-bleaching). Bleached, non-bleached, and background area are highlighted with solid, dashed, or dotted, white circles, respectively. Scale bar: 10 µm. For **a, c,** Nuclei were stained with DAPI. Scale bar: 20 µm. Right "zoom" panels show an enlarged view of the highlighted white boxed area in individual fluorescence channels and channels overlay (without DAPI).

Figure 5: MX2 condensate formation requires the N-terminal domain and dimerization and is regulated by TNPO1 and SAMD4A.

a, Right panel: Domain structure of MX2 with single amino acid mutations indicated. Disorder plot dSCOPE scores (y-axis) of MX2 (X-axis). Left panel: Disorder plots dSCOPE scores and Prion-like score (y-axis) of MX2 90 N-terminal amino acids (X-axis). Phase separation region, (NLS) according to [4], (PLD) according to PLAAC, and N-terminal MX2 deletion mutations are indicated. **b-d, f,** Parental HeLa (rtTA/tTS) cells and doxycycline-inducible HeLa cells expressing MX2(1-715) or mutant variants were treated with different doxycycline amounts to achieve comparable expression levels. **b,** Twenty-four hours after stimulation, cells were lysed and protein expression was analysed by immunoblot using anti-MX2 and anti-tubulin antibodies. **c,** Antiviral activities of MX2 mutant proteins against HSV-1 strain C12 and HIV-1-GFP**,** relative to HeLa MX2(1-715) samples which are each set to 100 (mean ± s.d., n = 5 independent experiments). **d,** Number of MX2 condensates (>0.1 μm^3 volume) per cell. **e,** HeLa cells expressing C-terminally EGFP-tagged MX2 proteins. **f,** Localization of V5-tagged MX2 proteins visualized using pseudocoloring blue to yellow gradient based upon intensity. **g,** HeLa cells (co)expressing LgBiT/FLAG-tagged MX2 mutants and SmBiT/V5-tagged LacZ, TNPO1, SAMD4A, and NUP35. Heat map representing reconstituted luminescence measurements for all the

combinations of LgBiT-, SmBiT-tagged proteins (mean ± s.d., n = 2 biological replicates). Protein expression was analysed by immunoblot using anti-FLAG, anti-V5, and anti-tubulin antibodies (see **Supplementary Fig.7g**). Representative experiment performed at least three times. **h,** Doxycycline-inducible HeLa MX2(1-715) C-terminally EGFP-tagged were transfected with 15 nM siRNAs. After 6 h, cells were stimulated with 100 ng mL^{-1} doxycycline. Number of MX2 condensates (>0.1 μm^3 volume) and % of large MX2 condensates (>2 μm^3 volume) per cell (mean ± s.d., two-tailed unpaired *t*-test to Non-Targeting siRNA; *p* values indicated with $*p < 0.05$, $**p < 0.01$, $***p < 0.001$). For **d, e, f, h,** Intracellular localization of MX2 was assessed 24 h (**d, e, f**) or 48 h (**h**) post-transfection by confocal microscopy. Nuclei were stained with DAPI. Scale bar: 20 µm. Bottom "zoom" panels show an enlarged view of the highlighted area (without DAPI). For **d, h,** cells were analysed by confocal microscopy with z-series image acquisition. For each comparison, either **d,** 54 cells or **h,** 96 cells were randomly selected.

Figure 6: MX2 condensates mimic the NPC LLPS environment to interact with incoming HIV-1 and HSV-1 capsids at different steps of their journey towards the nucleus.

a, c, Parental HeLa (rtTA/tTS) and doxycycline-inducible HeLa cells expressing MX2(1-715) or mutant MX2 variants, either **a,** EGFP- or **c,** V5-tagged were treated with different doxycycline amounts to achieve comparable expression levels. **b,** HeLaP4 cells expressing MX2(1-715)-mScarlet. Twenty-four hours after stimulation/transfection, cells were infected with **a,** HIV-1 based lentiviral vector (MOI:25) or **b,** HSV-1 (MOI:50) or **c,** HIV IN-EGFP. **a, b, c,** Intracellular localization of the MX2 proteins and incoming viral capsids or HIV-1 particles was assessed (**a)** 6 h.p.i. (**b)** 2.5 h.p.i. (**c)** 6 h.p.i. respectively by confocal microscopy. C: cytoplasm, N: nuclear membrane. z1, z2: z-slice 1, 2. Incoming viral capsids or HIV-1 particles colocalizing with MX2 condensates are indicated with white arrows. **c,** Right panel: total intracellular HSV-1 capsid number and percentage of HSV-1 capsids coinciding with the nuclear staining per cell. For each comparison, 44 cells were randomly selected (mean ± s.d., two-tailed unpaired *t*-test to cells without MX2; *p* values indicated with $*p < 0.05$, $**p < 0.01$, $***p < 0.001$). **d,** HeLa cells expressing MX2(1-715)-EGFP infected with HIV-1 based lentiviral vector from **Supplementary Fig.9b**. **e,** HeLa MX2(1-715)-V5 cells infected with HSV-1 from **Fig.6b**. **d, e,** Single z-slice view of the complete cell. Middle panels: enlarged view of the highlighted area in individual fluorescence channels and channel overlay, represented as 3D volume reconstruction. Right panels: graphs showing the **c,** HIV-1[43] **d,** HSV-1[42] capsids NPC association. Figures created with BioRender software. **f,** HeLa cells expressing MX2-EGFP. Intracellular localization of MX2-EGFP

and alpha-tubulin were assessed 24 h post-transfection by confocal microscopy. MX2 condensates colocalizing with MTs are indicated with white arrows. **g, h,** Antiviral experiments preformed at HeLa MX2 cells for **g,** HIV-1-GFP and **h,** HSV-1 firefly reporter virus in the presence of DMSO or 1, 5, or 10 µM nocodazole. Data analysis similar to **Supplementary Fig.4d and e**. **i,** HeLa cells expressing IPO4-mScarlet and EGFP-tagged MX2(1-715) or mutant MX2 variants. Intensity profile graphs of IPO4 and MX2. For **b-e,** cells were analysed by confocal microscopy with z-series image acquisition. Nuclei were stained with (**a, c, d, e, i,)** DAPI or **(b,)** NucSpot 650/665. Scale bar: **a-e,** 10 µm; **f, i,** 20 µm.

Supplementary figure 1: Validation of MX2-T2A/MUTT2A-TurboID fusion proteins.

a, Expression of MX2-T2A or MUTT2A-TurboID constructs. Upper panel: Design of the three plasmids used for the validation of MX2-TurboID fusion proteins, showing the CDS of the untagged MX2 and the MX2-T2A or MUTT2A-TurboID expression constructs. Lower panel: Transfected HEK293T cells expressing either the untagged MX2 or one of the MX2-T2A or MUTT2A-TurboID were lysed and proteins were analysed by immunoblot using anti-MX2 and anti-V5 antibodies. **b,** Interaction of MX2-MUTT2A-TurboID with FLAG-MX2. Transfected HEK293T cells expressing N-terminally FLAG-tagged MX2 together with MX2-MUTT2A-TurboID were lysed and proteins were immunoprecipitated (IP) in the presence or absence of anti-FLAG antibody. Co-immunoprecipitation of MX2-MUTT2A-TurboID was analysed by immunoblot using anti-MX2, anti-V5 and anti-tubulin antibodies. **c,** HeLa cells either mock-transfected or expressing MX1, MX2, or one of the MX2-T2A or MUTT2A-TurboID fusion proteins were mock-infected or infected with HSV-1 strain C12 (MOI:0.05). Viral growth was determined by real-time quantification of GFP signal every 24 h until 72 h.p.i. Upper panel: Data points indicate the green GFP fluorescent intensity normalized by subtracting the mean intensity of the mock-infected samples (mean ± s.d., n = 4 biological replicates). Middle panel: Relative area under the curve (AUC) from 0 h to 72 h.p.i. was calculated for each condition. AUC are relative to mock-transfected samples which are each set to 1 (mean ± s.d., n = 3 independent experiments, two-tailed unpaired *t*-test to mock-transfected condition; *p* values indicated with $*p < 0.05$, $**p < 0.01$, $***p < 0.001$, and $****p < 0.0001$). a.u., arbitrary units. Lower panel: Transfected or mock-transfected, infected HeLa cells were lysed 48 h.p.i and cellular and HSV-1 proteins were analysed by immunoblot using anti-MX2, anti-V5, anti-tubulin and anti-NC-1(VP5) antibodies. **d,** HeLa and U87-MG cells either mock-transfected or expressing MX2-T2A-TurboID or MX2-MUTT2A-TurboID. Intracellular localization of the V5-

tagged TurboID protein was assessed 24 h post-transfection by confocal microscopy. Nuclei were stained with DAPI. Scale bar: 20 µm

Supplementary figure 2: MX2 ''T2A spilt-link design'' BioID screening set up.

a, Doxycycline-inducible U87-MG MX2-T2A-TurboID and U87-MG MX2-MUTT2A-TurboID cells were mock-stimulated or stimulated with 5, 15, 50, 250 or 500 ng mL^{-1} doxycycline. Twenty-four hours after stimulation, biotin (50 µM) was added to the cells. Cells were lysed 2 h after biotin addition and proteins were analysed by immunoblot using anti-MX2, anti-V5, anti-tubulin antibodies. The biotinylation pattern in each condition was assessed on the same immunoblot using Alexa Fluor™ 680 streptavidin antibody. The doxycycline amounts used for the MS experiments are indicated with black arrows. **b,** Schematic representation of the MX2 ''T2A spilt-link design'' proximity biotinylation (BioID) screening. MX2 BioID was performed in three different conditions (-IFN, +IFN, and HSV-1). U87-MG MX2-T2A-TurboID and U87-MG MX2-MUTT2A-TurboID cell lines were stimulated with 15 ng mL^{-1} doxycycline for 24 h, in the absence or presence of 1000 IU mL^{-1} human IFNα2α, followed by the addition of 50 µM biotin for 2 h to biotinylate proteins in the proximity of free or MX2 linked TurboID, respectively. For the HSV-1 infected samples, biotin was added simultaneously with HSV-1 strain F infection (MOI:20). After cell lysis, biotinylated proteins were enriched on streptavidin-conjugated beads and digested by trypsin on the beads. The resulting peptides were identified and quantified by LC-MS/MS analysis. Figure created with BioRender software. **c,** Profile plot of MX2 (cyan), V5-TurboID (orange) and three housekeeping proteins, VIM, GAPDH and EEF1A1 (different shades of purple), showing log2(LFQ Intensity) values for each individual MX2-T2A-TurboID and MX2-MUTT2A-TurboID MS sample across all three MX2 BioID conditions.

Supplementary figure 3: MX2 associates with mitochondrial and coated vesicles proteins, besides nuclear transport proteins and granule-associated ribonucleoproteins.

a, Bar charts showing the top 10 Gene Ontology (GO) terms for biological process (upper panel) and cellular components (bottom panel), ranked by -log10(adjusted p-value) of the commonly enriched MX2 interactors. **b,** Upper panel: Nodes and edges of the SAFE enriched ''mitochondrial containing-protein complex'' domain, selected and visualized as a separate protein network. Lower panel: Dotplot of mitochondrial containing-protein complex domain proteins ranked according to their average enrichment (log2(FC)) in all three conditions. Endogenously biotinylated mitochondrial proteins that are known BioID contaminants are indicated with a red exclamation mark. **c,** Upper panel: Nodes and edges of the SAFE enriched

''coated vesicle'' domain, selected and visualized as a separate protein network. Lower panel: Dotplot of coated vesicle domain proteins ranked according to their average enrichment (log2(FC)) in all three conditions. **d,** Nodes and edges of the SAFE enriched ''granule ribonucleoprotein domain'', selected and visualized as a separate protein network.

Supplementary figure 4: Knockdown of SAMD4A, TNPO1, and NUP35 affects MX2-mediated antiviral activity against HIV-1 and HSV-1.

a, Doxycycline-inducible HeLa MX2 cells were mock-stimulated or stimulated with 5, 15, 50, or 250 ng mL^{-1} doxycycline. Twenty-four hours after induction, cells were lysed and protein expression was analysed by immunoblot using anti-MX2 and anti-tubulin antibodies. **b,** RT-qPCR data showing relative to Non-Targeting expression mRNA levels of each targeted gene at HeLa MX2 cells 24 h after transfection with the indicated SMARTpool siRNAs. **c,** Flow cytometry gating strategy following RNAi and HIV-1-GFP transduction. Cells were gated using the forward scatter (FSC) and side scatter (SSC). Single cells were selected using FSC-H and FSC-A. GFP+ population was gated using uninfected cells as negative control. Representative plots showing GFP+ cells for Non-Targeting siRNA samples with and without doxycycline stimulation are shown. **d-e,** HeLa MX2 cells were transfected with combinations of 15 nM siRNA (total 30 nM) targeting individual MX2 BioID identified protein genes. Six hours after siRNA transfection, cells were left untreated or were induced with 100 ng mL^{-1} doxycycline. **d,** Left panel: 48 h after transfection, cells were infected with HSV-1 firefly reporter virus (MOI:1). Cells were lysed 6.5 h.p.i. and luminescence was measured. Results are shown relative to the Non-Targeting (-doxy) condition. Protein expression was analysed by immunoblot using anti-MX2, and anti-tubulin antibodies. Right panel: Fold MX2-mediated HSV-1 inhibition was calculated by dividing luminescence of the untreated by the doxycycline-induced samples in each condition (mean ± s.d., n = 4 independent experiments, two-tailed paired *t*-test to Non-Targeting siRNA; *p* values indicated with $*p < 0.05$, $**p < 0.01$, $***p < 0.001$). **e,** Left panel: 48 h after transfection, cells were challenged with HIV-1-GFP (MOI:0.4). Transduction efficiency was assessed 48 h post-challenge by flow-cytometry. Right panel: Fold MX2-mediated HIV-1 inhibition was calculated by dividing % GFP+ cells of the untreated by the doxycycline-induced samples in each condition (mean ± s.d., n = 4 independent experiments, two-tailed paired *t*-test to Non-Targeting siRNA, indicate *p* values with $*p < 0.05$, $**p < 0.01$, $***p < 0.001$).

Supplementary figure 5: Bleed-through controls for live cell imaging, multicolor confocal microscopy and FRAP.

a, Live-cell imaging **c,** FRAP experiments. **a, c,** HeLa cells were mock-transfected or expressing MX2 tagged either with EGFP or mScarlet and were imaged 24 h post-transfection under time-lapse conditions. Laser power and detection window were set to avoid spectral bleed-through between the different fluorophores. Scale bar: 10 µm. **b,** HeLa cells mock-transfected or transiently expressing MX2 tagged either with V5, EGFP or mScarlet. Intracellular localization of the MX2 proteins was assessed 24 h post-transfection by confocal microscopy with laser power set to avoid spectral bleed-through between the different fluorophores. Nuclei were stained with DAPI. Scale bar: 20 µm.

Supplementary figure 6: MX2 condensates interact with PBs and SGs and comprise RNA binding or/and disordered domain proteins.

a, HeLa cells mock-transfected or expressing EGFP-tagged LSM14A in the presence or absence of MX2-V5. Intracellular localization of the EGFP- and V5-tagged proteins were assessed 24 h post- transfection by confocal microscopy. **b,** HeLa cells expressing MX2-mScarlet together with EGFP-tagged LSM14A were imaged under time-lapse conditions. **c,** HeLa cells mock-transfected or expressing EGFP-tagged G3BP1 in the presence or absence of V5-tagged MX2. Twenty-four hours post-transfection, cells were mock-treated or treated with 500 µM of sodium arsenite ($NaAsO_2$) for 45mins. Intracellular localization of the EGFP- and V5-tagged proteins were assessed by confocal microscopy. **d,** HeLa cells expressing NUPL1-V5, MX2-mScarlet and EGFP-tagged SAMD4B, FUBP3, or CNOT4. Twenty-four hours post-transfection intracellular localization of the V5-, mScarlet-, and GFP-tagged proteins was assessed by confocal microscopy. **f,** HeLa cells expressing MX2-mScarlet together with EGFP-tagged SAMD4B or FUBP3 were imaged under time-lapse conditions. **g,** HeLa cells expressing EGFP-tagged SAMD4B or FUBP3, together with MX2-mScarlet. FRAP was performed for the complete individual condensates 24 h post-transfection. Upper panel: Normalized FRAP curves obtained for EGFP signal over time (n=7). Plateau and half-time are indicated on the right of each curve. Bottom panel: Representative images showing the biomolecular condensates during FRAP (before, during, and 34 and 84 sec post-bleaching). Bleached, non-bleached, and background area are highlighted with solid, dashed or dotted, white circles, respectively. Scale bar: 10 µm. For **a, c, d, e** Nuclei were stained with DAPI. Scale bar: 20 µm. Right "zoom" panels show an enlarged view of the highlighted white boxed area in individual fluorescence channels and channels overlay (without DAPI). For **b, f,** Bottom "zoom" panels show an enlarged view of the highlighted white boxed area. Moving and fusing MX2

condensates are indicated with white arrows. Real time of imaging is indicated at the bottom left side of each image. Scale bar: 10 µm.

Supplementary figure 7: MX2 N-terminal disordered domain and dimerization are required for condensate formation and anti-HIV-1 and -HSV-1 antiviral activity.

a, Disorder plot FuzDrop Droplet Promoting (pDP) scores (y-axis) of MX2 (X-axis). **b,** Disorder plot IUPred2 scores in purple and ANCHOR scores in blue (y-axis) of MX2 (X-axis). **c,** Prion-like domain prediction for MX2 using PLAAC. Upper panel: Disorder plot represents the predicted tendency to form a prion-like domain. Bottom panel: MX2 amino acids sequence with the predicted prion-like domain indicated in red. **d, e,** Doxycycline-inducible HeLa MX2(1-715) and mutants C-terminally V5- tagged were treated with different doxycycline amounts to achieve comparable expression levels. **d,** Forty-eight hours after stimulation, cells were challenged with HIV-1-GFP (MOI:0.2). Transduction efficiency was assessed 48 h post-challenge by flow-cytometry. % GFP+ cells of each HeLa MX2 cell line are shown relative to HeLa MX2(1-715) samples which are each set to 100 (mean ± s.d., n = 5 independent experiments). Flow cytometry gating strategy: cells were gated using the forward scatter (FSC) and side scatter (SSC). Single cells were selected using FSC-H and FSC-A. GFP+ population was gated using uninfected cells as negative control. Representative plots showing MX2(1-715) and MX2(M574D) are shown. **e,** Twenty-four hours after stimulation, cells were challenged with HSV-1 strain C12 (MOI:0.05). Viral growth was determined by real-time quantification of GFP signal every 24 h until 72 h.p.i. Upper panel: Data points indicate the green GFP fluorescent intensity normalized to the mean intensity of the mock-infected samples (mean ± s.d., n = 4 biological replicates). a.u., arbitrary units. Lower panel: Relative area under the curve (AUC) from 0 h to 72 h.p.i. was calculated for each HeLa MX2 cell line. AUC are relative to HeLa MX2(1-715) samples which are each set to 100 (mean ± s.d., n = 5 independent experiments). **f,** HeLa cells expressing C-terminally EGFP-tagged MX2(1-715) and mutants. Intracellular localization of the EGFP-tagged proteins were assessed 24 h post-transfection by confocal imaging. Scale bar: 20 µm. Bottom "zoom" panels show an enlarged view of the highlighted white boxed area (without DAPI).

Supplementary figure 8: Doxycycline-inducible HeLa MX2 C-terminally EGFP-tagged cell lines.

a-b-c, Paternal HeLa (rtTA/tTS) cells and doxycycline-inducible HeLa MX2(1-715), MX2(26-715), and MX2(T151A) C-terminally EGFP-tagged cells were treated with different doxycycline

amounts to achieve comparable expression levels. **a,** Twenty-four hours after induction, cells were lysed and protein expression was analysed by immunoblot using anti-EGFP and anti-tubulin antibodies. **b,** Intracellular localization of the EGFP-tagged MX2 proteins was assessed 24 h post-induction by confocal imaging. **c**, Intracellular localization of EGFP-tagged MX2 proteins and alpha-tubulin were assessed 24 h post-induction by confocal microscopy. Nuclei were stained with DAPI. Scale bar: 20 µm.

Supplementary figure 9: MX2 condensates interact with incoming HIV-1 and HSV-1 capsids supplementary information.

a, Parental HeLa (rtTA/tTS) and doxycycline-inducible HeLa MX2(1-715) or (26-715) C-terminally EGFP- tagged cells were treated with different doxycycline amounts to achieve comparable expression levels. Twenty-four hours after induction, cells were mock-infected or challenged with HIV-1 based lentiviral vector (MOI:25). Six hours after transduction, intracellular localization of the MX2 proteins and incoming HIV-1 capsids was assessed by confocal microscopy using anti-p24 HIV-1 clone *[AG3.0]* antibody. **b,** HeLa cells mock-transfected or expressing MX2(1-715)-EGFP. Twenty-four hours post-transfection, cells were mock-infected or challenged with HIV-1 based lentiviral vector (MOI:25). Six hours after transduction, intracellular localization of the MX2 proteins and incoming HIV-1 capsids was assessed by confocal microscopy using anti-p24 HIV-1 clone [*39/5.4A]* antibody. Right "zoom" panel show an enlarged view of the highlighted white boxed area in channels overlay (with DAPI). Incoming HIV-1 capsids colocalizing with MX2 condensates are indicated with white arrows. **c,** HeLaP4 cells expressing C-terminally mScarlet-tagged MX2(1-715) were mock-infected or infected with HIV IN-EGFP. Six hours after transduction, intracellular localization of the MX2 proteins and incoming HIV-1 particles was assessed by confocal microscopy. Right "zoom" panel show an enlarged view of the highlighted white boxed area in channels overlay (with DAPI). Incoming HIV-1 particles colocalizing with MX2 condensates are indicated with white arrows. **d,** Parental HeLa (rtTA/tTS) and doxycycline-inducible HeLa MX2(1-715), (26-715), or (K131A) C-terminally V5-tagged cells were treated with different doxycycline amounts to achieve comparable expression levels. Twenty-four hours after induction, cells were mock-infected or challenged with HSV-1 infection (MOI:50). Two and a half hours after infection, intracellular localization of the MX2 proteins and incoming viral capsids was assessed by confocal microscopy using anti-V5 and anti-HSV-1 capsid (SY4563, anti-capsid) antibodies. For **b-d,** cells were analysed by confocal microscopy with z-series image acquisition. Images of single z-slice view of the complete cell are shown. For **a-d,** the laser power was set to avoid

spectral bleed-through between the different fluorophores. For **a,b,d** nuclei were stained with DAPI **c,** with NucSpot 650/665. Scale bar: 10 µm.

Supplementary figure 10: MX2 condensates interact with incoming HIV-1 and HSV-1 capsids at different steps of their journey towards the nucleus.

a, HeLa cells mock-transfected or expressing MX2(1-715)-GFP, intracellular localization of MX2-GFP and alpha-tubulin were assessed 24 h post-transfection by confocal microscopy in the presence or absence of anti-alpha-tubulin antibody. The laser power was set to avoid spectral bleed-through between the different fluorophores. **b,** HeLa cells expressing MX2(1-715)-EGFP. Twenty-four hours post-transfection, cells were either mock-treated with DMSO or treated with 1, 5, or 10 µM of nocodazole. Intracellular localization of MX2-EGFP and tubulin depolymerization were assessed 3 h after treatment by immunostaining using anti-alpha-tubulin antibody. **c,** Doxycycline-inducible HeLa MX2 cells were left untreated or were induced with 100 ng mL^{-1} doxycycline. After 48 h, cells were either mock-treated with DMSO or treated with 1, 5, or 10 µM of nocodazole. Three hours post-treatment cells were challenged with HIV-1-GFP in the presence of similar DMSO or nocodazole treatment for 7 h before medium was refreshed with normal growth medium. Transduction efficiency was assessed 48 h post-challenge by flow-cytometry. Flow cytometry gating strategy following nocodazole treatment. Cells were gated using the forward scatter (FSC) and side scatter (SSC). Single cells were selected using FSC-H and FSC-A. GFP+ population was gated using uninfected cells as negative control. Representative plots showing GFP+ cells for DSMO mock-treated samples with and without doxycycline stimulation is shown. **d,** HeLa cells mock-transfected or expressing mScarlet-tagged IPO4 or EGFP-tagged MX2(1-715). intracellular localization of the EGFP- and mScarlet-tagged proteins were assessed 24 h post-transfection by immunostaining. The laser power was set to avoid spectral bleed-through between the different fluorophores. For **a, b,** nuclei were stained with DAPI. Scale bar: 20 µm.

Supplementary video legends

Sup.Video.1. LIVE_MX2-EGFP: HeLa cells transiently expressing C-terminally EGFP-tagged MX2(1-715) imaged under time-lapse conditions.

Sup.Video.2. LIVE_SAMD4A-EGFP + MX2-mScarlet: HeLa cells transiently expressing C-terminally EGFP-tagged SAMD4A together with C-terminally mScarlet-tagged MX2(1-715) imaged under time-lapse conditions.

Sup.Video.3. LIVE_TNPO1-EGFP + MX2-mScarlet: HeLa cells transiently expressing C-terminally EGFP-tagged TNPO1 together with C-terminally mScarlet-tagged MX2(1-715) imaged under time-lapse conditions.

Sup.Video.4. LIVE_NUP35-EGFP + MX2-mScarlet: HeLa cells transiently expressing C-terminally EGFP-tagged NUP35 together with C-terminally mScarlet-tagged MX2(1-715) imaged under time-lapse conditions.

Sup.Video.5. LIVE_NUPL1-EGFP + MX2-mScarlet: HeLa cells transiently expressing C-terminally EGFP-tagged NUPL1 together with C-terminally mScarlet-tagged MX2(1-715) imaged under time-lapse conditions.

Sup.Video.6. LIVE_IPO4-EGFP + MX2-mScarlet: HeLa cells transiently expressing C-terminally EGFP-tagged IPO4 together with C-terminally mScarlet-tagged MX2(1-715) imaged under time-lapse conditions.

Sup.Video.7. LIVE_LSM14A-EGFP + MX2-mScarlet: HeLa cells transiently expressing C-terminally EGFP-tagged LSM14A together with C-terminally mScarlet-tagged MX2(1-715) imaged under time-lapse conditions.

Sup.Video.8. LIVE_SAMD4B-EGFP + MX2-mScarlet: HeLa cells transiently expressing C-terminally EGFP-tagged SAMD4B together with C-terminally mScarlet-tagged MX2(1-715) imaged under time-lapse conditions.

Sup.Video.9. LIVE_FUBP3-EGFP + MX2-mScarlet: HeLa cells transiently expressing C-terminally EGFP-tagged FUBP3 together with C-terminally mScarlet-tagged MX2(1-715) imaged under time-lapse conditions.

Sup.Video.10. LIVE_MX2(Δ26-90): HeLa cells transiently expressing C-terminally EGFP-tagged MX2(Δ26-90) imaged under time-lapse conditions.

Sup.Video.11. LIVE_MX2(1-715): HeLa cells transiently expressing C-terminally EGFP-tagged MX2(1-715) imaged under time-lapse conditions.

Sup.Video.12. LIVE_MX2(26-715): HeLa cells transiently expressing C-terminally EGFP-tagged MX2(26-715) imaged under time-lapse conditions.

Sup.Video.13. LIVE_MX2(51-715): HeLa cells transiently expressing C-terminally EGFP-tagged MX2(51-715) imaged under time-lapse conditions.

Sup.Video.14. LIVE_MX2(Δ26-50): HeLa cells transiently expressing C-terminally EGFP-tagged MX2(Δ26-50) imaged under time-lapse conditions.

Sup.Video.15. LIVE_MX2(K131A): HeLa cells transiently expressing C-terminally EGFP-tagged MX2(K131A) imaged under time-lapse conditions.

Sup.Video.16. LIVE_MX2(M574D): HeLa cells transiently expressing C-terminally EGFP-tagged MX2(M574D) imaged under time-lapse conditions.

Sup.Video.17. LIVE_MX2(L666D): HeLa cells transiently expressing C-terminally EGFP-tagged MX2(L666D) imaged under time-lapse conditions.

Sup.Video.18. LIVE_MX2(T151A): HeLa cells transiently expressing C-terminally EGFP-tagged MX2(T151A) imaged under time-lapse conditions.

References

1. Schoggins, J. W. *et al.* A diverse range of gene products are effectors of the type I interferon antiviral response. *Nature* **472**, 481–485 (2011).
2. Mesev, E. V., LeDesma, R. A. & Ploss, A. Decoding type I and III interferon signalling during viral infection. *Nat Microbiol* **4**, 914–924 (2019).
3. Haller, O., Arnheiter, H., Pavlovic, J. & Staeheli, P. The Discovery of the Antiviral Resistance Gene Mx: A Story of Great Ideas, Great Failures, and Some Success. *Annu Rev Virol* **5**, 33–51 (2018).
4. Schulte, B. *et al.* Restriction of HIV-1 Requires the N-Terminal Region of MxB as a Capsid-Binding Motif but Not as a Nuclear Localization Signal. *J. Virol.* **89**, 8599–8610 (2015).
5. Goujon, C. *et al.* Human MX2 is an interferon-induced post-entry inhibitor of HIV-1 infection. *Nature* **502**, 559–562 (2013).
6. Kane, M. *et al.* MX2 is an interferon-induced inhibitor of HIV-1 infection. *Nature* **502**, 563–566 (2013).
7. Liu, Z. *et al.* The interferon-inducible MxB protein inhibits HIV-1 infection. *Cell Host Microbe* **14**, 398–410 (2013).
8. Serrero, M. C. *et al.* The interferon-inducible GTPase MxB promotes capsid disassembly and genome release of herpesviruses. *Elife* **11**, e76804 (2022).
9. Schilling, M. *et al.* Human MxB Protein Is a Pan-herpesvirus Restriction Factor. *J Virol* **92**, e01056-18 (2018).
10. Jaguva Vasudevan, A. A. *et al.* MXB inhibits murine cytomegalovirus. *Virology* **522**, 158–167 (2018).
11. Crameri, M. *et al.* MxB is an interferon-induced restriction factor of human herpesviruses. *Nat Commun* **9**, 1980 (2018).
12. Staeheli, P. & Haller, O. Human MX2/MxB: a Potent Interferon-Induced Postentry Inhibitor of Herpesviruses and HIV-1. *J Virol* **92**, e00709-18 (2018).
13. Ren, Y. *et al.* High accumulation of Mx2 renders limited multiplication of oncolytic herpes simplex virus-1 in human tumor cells. *Sci Rep* **11**, 21227 (2021).
14. Yi, D.-R. *et al.* Human MxB Inhibits the Replication of Hepatitis C Virus. *J Virol* **93**, e01285-18 (2019).
15. Li, Q. *et al.* MxB Disrupts Hepatitis C Virus NS5A-CypA Complex: Insights From a Combined Theoretical and Experimental Approach. *Front Microbiol* **13**, 849084 (2022).

16. Wang, Y.-X. *et al.* Interferon-inducible MX2 is a host restriction factor of hepatitis B virus replication. *J Hepatol* **72**, 865–876 (2020).
17. Cao, H. *et al.* The anti-viral dynamin family member MxB participates in mitochondrial integrity. *Nat Commun* **11**, 1048 (2020).
18. Huang, Y. *et al.* MxB inhibits long interspersed element type 1 retrotransposition. *PLoS Genet* **18**, e1010034 (2022).
19. Ramachandran, R. & Schmid, S. L. The dynamin superfamily. *Current Biology* **28**, R411–R416 (2018).
20. Fribourgh, J. L. *et al.* Structural insight into HIV-1 restriction by MxB. *Cell Host Microbe* **16**, 627–638 (2014).
21. Matreyek, K. A. *et al.* Host and viral determinants for MxB restriction of HIV-1 infection. *Retrovirology* **11**, 90 (2014).
22. Buffone, C., Schulte, B., Opp, S. & Diaz-Griffero, F. Contribution of MxB oligomerization to HIV-1 capsid binding and restriction. *J. Virol.* **89**, 3285–3294 (2015).
23. Dicks, M. D. J. *et al.* Oligomerization Requirements for MX2-Mediated Suppression of HIV-1 Infection. *J. Virol.* **90**, 22–32 (2016).
24. Mitchell, P. S., Young, J. M., Emerman, M. & Malik, H. S. Evolutionary Analyses Suggest a Function of MxB Immunity Proteins Beyond Lentivirus Restriction. *PLoS Pathog.* **11**, e1005304 (2015).
25. Goujon, C. *et al.* Transfer of the amino-terminal nuclear envelope targeting domain of human MX2 converts MX1 into an HIV-1 resistance factor. *J Virol* **88**, 9017–9026 (2014).
26. Goujon, C., Greenbury, R. A., Papaioannou, S., Doyle, T. & Malim, M. H. A triple-arginine motif in the amino-terminal domain and oligomerization are required for HIV-1 inhibition by human MX2. *J. Virol.* **89**, 4676–4680 (2015).
27. Lee, J., Cho, H. & Kwon, I. Phase separation of low-complexity domains in cellular function and disease. *Exp Mol Med* **54**, 1412–1422 (2022).
28. Dignon, G. L., Best, R. B. & Mittal, J. Biomolecular Phase Separation: From Molecular Driving Forces to Macroscopic Properties. *Annu Rev Phys Chem* **71**, 53–75 (2020).
29. Hirose, T., Ninomiya, K., Nakagawa, S. & Yamazaki, T. A guide to membraneless organelles and their various roles in gene regulation. *Nat Rev Mol Cell Biol* 1–17 (2022) doi:10.1038/s41580-022-00558-8.
30. Li, P. *et al.* Phase transitions in the assembly of multivalent signalling proteins. *Nature* **483**, 336–340 (2012).

31. Riback, J. A. *et al.* Stress-Triggered Phase Separation Is an Adaptive, Evolutionarily Tuned Response. *Cell* **168**, 1028-1040.e19 (2017).
32. Roux, K. J., Kim, D. I. & Burke, B. BioID: a screen for protein-protein interactions. *Curr Protoc Protein Sci* **74**, Unit 19.23. (2013).
33. Branon, T. C. *et al.* Efficient proximity labeling in living cells and organisms with TurboID. *Nat. Biotechnol.* (2018) doi:10.1038/nbt.4201.
34. Vandemoortele, G. *et al.* A Well-Controlled BioID Design for Endogenous Bait Proteins. *J Proteome Res* **18**, 95–106 (2019).
35. Dicks, M. D. J. *et al.* Multiple components of the nuclear pore complex interact with the amino-terminus of MX2 to facilitate HIV-1 restriction. *PLOS Pathogens* **14**, e1007408 (2018).
36. Betancor, G. *et al.* MX2-mediated innate immunity against HIV-1 is regulated by serine phosphorylation. *Nat Microbiol* **6**, 1031–1042 (2021).
37. Lemke, E. A. The Multiple Faces of Disordered Nucleoporins. *Journal of Molecular Biology* **428**, 2011–2024 (2016).
38. Konishi, H. A. & Yoshimura, S. H. Interactions between non-structured domains of FG- and non-FG-nucleoporins coordinate the ordered assembly of the nuclear pore complex in mitosis. *FASEB J* **34**, 1532–1545 (2020).
39. Celetti, G. *et al.* The liquid state of FG-nucleoporins mimics permeability barrier properties of nuclear pore complexes. *J Cell Biol* **219**, e201907157 (2019).
40. Baez, M. V. & Boccaccio, G. L. Mammalian Smaug is a translational repressor that forms cytoplasmic foci similar to stress granules. *J Biol Chem* **280**, 43131–43140 (2005).
41. Youn, J.-Y. *et al.* High-Density Proximity Mapping Reveals the Subcellular Organization of mRNA-Associated Granules and Bodies. *Mol Cell* **69**, 517-532.e11 (2018).
42. Döhner, K., Cornelius, A., Serrero, M. C. & Sodeik, B. The journey of herpesvirus capsids and genomes to the host cell nucleus. *Curr Opin Virol* **50**, 147–158 (2021).
43. Temple, J., Tripler, T. N., Shen, Q. & Xiong, Y. A snapshot of HIV-1 capsid–host interactions. *Curr Res Struct Biol* **2**, 222–228 (2020).
44. King, M. C., Raposo, G. & Lemmon, M. A. Inhibition of nuclear import and cell-cycle progression by mutated forms of the dynamin-like GTPase MxB. *Proc Natl Acad Sci U S A* **101**, 8957–8962 (2004).
45. Fernández-Alvarez, A. J. *et al.* Smaug1 membrane-less organelles respond to AMPK and mTOR and affect mitochondrial function. *J Cell Sci* **135**, jcs253591 (2022).

46. Wang, Z., Lou, J. & Zhang, H. Essence determines phenomenon: Assaying the material properties of biological condensates. *Journal of Biological Chemistry* **298**, 101782 (2022).
47. Yu, M. *et al.* Visualizing the disordered nuclear transport machinery in situ. *Nature* **617**, 162–169 (2023).
48. Frey, S., Richter, R. P. & Görlich, D. FG-Rich Repeats of Nuclear Pore Proteins Form a Three-Dimensional Meshwork with Hydrogel-Like Properties. *Science* **314**, 815–817 (2006).
49. Aramburu, I. V. & Lemke, E. A. Floppy but not sloppy: Interaction mechanism of FG-nucleoporins and nuclear transport receptors. *Seminars in Cell & Developmental Biology* **68**, 34–41 (2017).
50. Schmidt, H. B. & Görlich, D. Transport Selectivity of Nuclear Pores, Phase Separation, and Membraneless Organelles. *Trends in Biochemical Sciences* **41**, 46–61 (2016).
51. Yu, K. *et al.* dSCOPE: a software to detect sequences critical for liquid–liquid phase separation. *Briefings in Bioinformatics* **24**, bbac550 (2023).
52. Hardenberg, M., Horvath, A., Ambrus, V., Fuxreiter, M. & Vendruscolo, M. Widespread occurrence of the droplet state of proteins in the human proteome. *Proceedings of the National Academy of Sciences* **117**, 33254–33262 (2020).
53. Erdős, G. & Dosztányi, Z. Analyzing Protein Disorder with IUPred2A. *Current Protocols in Bioinformatics* **70**, e99 (2020).
54. Lancaster, A. K., Nutter-Upham, A., Lindquist, S. & King, O. D. PLAAC: a web and command-line application to identify proteins with prion-like amino acid composition. *Bioinformatics* **30**, 2501–2502 (2014).
55. Kane, M. *et al.* Nuclear pore heterogeneity influences HIV-1 infection and the antiviral activity of MX2. *Elife* **7**, e35738 (2018).
56. Guedán, A., Caroe, E. R., Barr, G. C. R. & Bishop, K. N. The Role of Capsid in HIV-1 Nuclear Entry. *Viruses* **13**, 1425 (2021).
57. Zila, V. *et al.* Cone-shaped HIV-1 capsids are transported through intact nuclear pores. *Cell* **184**, 1032-1046.e18 (2021).
58. Fay, N. & Panté, N. Nuclear entry of DNA viruses. *Front Microbiol* **6**, 467 (2015).
59. Naghavi, M. H. HIV-1 capsid exploitation of the host microtubule cytoskeleton during early infection. *Retrovirology* **18**, 19 (2021).
60. Koppers, M., Özkan, N. & Farías, G. G. Complex Interactions Between Membrane-Bound Organelles, Biomolecular Condensates and the Cytoskeleton. *Frontiers in Cell and Developmental Biology* **8**, (2020).

61. Sabo, Y. *et al.* HIV-1 Induces the Formation of Stable Microtubules to Enhance Early Infection. *Cell Host & Microbe* **14**, 535–546 (2013).
62. Mabit, H. *et al.* Intact Microtubules Support Adenovirus and Herpes Simplex Virus Infections. *Journal of Virology* **76**, 9962–9971 (2002).
63. Sodeik, B., Ebersold, M. W. & Helenius, A. Microtubule-mediated Transport of Incoming Herpes Simplex Virus 1 Capsids to the Nucleus. *J Cell Biol* **136**, 1007–1021 (1997).
64. Flatt, J. W. & Greber, U. F. Viral mechanisms for docking and delivering at nuclear pore complexes. *Semin Cell Dev Biol* **68**, 59–71 (2017).
65. Abaitua, F., Hollinshead, M., Bolstad, M., Crump, C. M. & O'Hare, P. A Nuclear localization signal in herpesvirus protein VP1-2 is essential for infection via capsid routing to the nuclear pore. *J Virol* **86**, 8998–9014 (2012).
66. Fare, C. M., Villani, A., Drake, L. E. & Shorter, J. Higher-order organization of biomolecular condensates. *Open Biol* **11**, 210137.
67. Ng, S. C. *et al.* Barrier properties of Nup98 FG phases ruled by FG motif identity and inter-FG spacer length. *Nat Commun* **14**, 747 (2023).
68. Schmidt, H. B. & Görlich, D. Nup98 FG domains from diverse species spontaneously phase-separate into particles with nuclear pore-like permselectivity. *eLife* **4**, e04251 (2015).
69. Steiner, F. & Pavlovic, J. Subcellular Localization of MxB Determines Its Antiviral Potential against Influenza A Virus. *J Virol* **94**, e00125-20 (2020).
70. Goujon, C. *et al.* Transfer of the Amino-Terminal Nuclear Envelope Targeting Domain of Human MX2 Converts MX1 into an HIV-1 Resistance Factor. *Journal of Virology* **88**, 9017–9026 (2014).
71. Hofweber, M. *et al.* Phase Separation of FUS Is Suppressed by Its Nuclear Import Receptor and Arginine Methylation. *Cell* **173**, 706-719.e13 (2018).
72. Qamar, S. *et al.* FUS Phase Separation Is Modulated by a Molecular Chaperone and Methylation of Arginine Cation-π Interactions. *Cell* **173**, 720-734.e15 (2018).
73. Guo, L. *et al.* Nuclear-Import Receptors Reverse Aberrant Phase Transitions of RNA-Binding Proteins with Prion-like Domains. *Cell* **173**, 677-692.e20 (2018).
74. Yoshizawa, T. *et al.* Nuclear Import Receptor Inhibits Phase Separation of FUS through Binding to Multiple Sites. *Cell* **173**, 693-705.e22 (2018).
75. Betancor, G. *et al.* MX2 Viral Substrate Breadth and Inhibitory Activity Are Regulated by Protein Phosphorylation. *mBio* **13**, e0171422 (2022).

76. Li, J. *et al.* Post-translational modifications in liquid-liquid phase separation: a comprehensive review. *Mol Biomed* **3**, 13 (2022).
77. López-Palacios, T. P. & Andersen, J. L. Kinase regulation by liquid–liquid phase separation. *Trends in Cell Biology* **0**, (2022).
78. Betancor, G. *et al.* The GTPase Domain of MX2 Interacts with the HIV-1 Capsid, Enabling Its Short Isoform to Moderate Antiviral Restriction. *Cell Rep* **29**, 1923-1933.e3 (2019).
79. Fricke, T. *et al.* MxB binds to the HIV-1 core and prevents the uncoating process of HIV-1. *Retrovirology* **11**, (2014).
80. Xie, L. *et al.* GTPase Activity of MxB Contributes to Its Nuclear Location, Interaction with Nucleoporins and Anti-HIV-1 Activity. *Virol Sin* **36**, 85–94 (2021).
81. Miles, R. J. *et al.* MxB sensitivity of HIV-1 is determined by a highly variable and dynamic capsid surface. *Elife* **9**, e56910 (2020).
82. Lee, K. *et al.* Flexible Use of Nuclear Import Pathways by HIV-1. *Cell Host & Microbe* **7**, 221–233 (2010).
83. Goujon, C. *et al.* Human MX2 is an interferon-induced post-entry inhibitor of HIV-1 infection. *Nature* **502**, 559–562 (2013).
84. Schaller, T. *et al.* HIV-1 Capsid-Cyclophilin Interactions Determine Nuclear Import Pathway, Integration Targeting and Replication Efficiency. *PLOS Pathogens* **7**, e1002439 (2011).
85. Lin, Y.-C. *et al.* Genome dynamics of the human embryonic kidney 293 lineage in response to cell biology manipulations. *Nat Commun* **5**, 4767 (2014).
86. Mondor, I., Ugolini, S. & Sattentau, Q. J. Human Immunodeficiency Virus Type 1 Attachment to HeLa CD4 Cells Is CD4 Independent and gp120 Dependent and Requires Cell Surface Heparans. *J Virol* **72**, 3623–3634 (1998).
87. Albanese, A., Arosio, D., Terreni, M. & Cereseto, A. HIV-1 Pre-Integration Complexes Selectively Target Decondensed Chromatin in the Nuclear Periphery. *PLOS ONE* **3**, e2413 (2008).
88. Borrenberghs, D. *et al.* Dynamic Oligomerization of Integrase Orchestrates HIV Nuclear Entry. *Sci Rep* **6**, 36485 (2016).
89. Adachi, A. *et al.* Production of acquired immunodeficiency syndrome-associated retrovirus in human and nonhuman cells transfected with an infectious molecular clone. *Journal of Virology* **59**, 284–291 (1986).
90. Grosche, L. *et al.* Herpes Simplex Virus Type 1 Propagation, Titration and Single-step Growth Curves. *Bio-protocol* e3441–e3441 (2019).

91. Glauser, D. L. *et al.* Inhibition of herpes simplex virus type 1 replication by adeno-associated virus rep proteins depends on their combined DNA-binding and ATPase/helicase activities. *J Virol* **84**, 3808–3824 (2010).
92. Khadivjam, B. *et al.* The ATP-Dependent RNA Helicase DDX3X Modulates Herpes Simplex Virus 1 Gene Expression. *J Virol* **91**, e02411-16 (2017).
93. Sandbaumhüter, M. *et al.* Cytosolic herpes simplex virus capsids not only require binding inner tegument protein pUL36 but also pUL37 for active transport prior to secondary envelopment. *Cellular Microbiology* **15**, 248–269 (2013).
94. Cohen, G. H. *et al.* Structural analysis of the capsid polypeptides of herpes simplex virus types 1 and 2. *J Virol* **34**, 521–531 (1980).
95. Döhner, K. *et al.* Importin α1 is required for nuclear import of herpes simplex virus proteins and capsid assembly in fibroblasts and neurons. *PLoS Pathog* **14**, e1006823 (2018).
96. Shannon, P. *et al.* Cytoscape: a software environment for integrated models of biomolecular interaction networks. *Genome Res* **13**, 2498–2504 (2003).
97. Baryshnikova, A. Systematic Functional Annotation and Visualization of Biological Networks. *Cell Syst* **2**, 412–421 (2016).
98. Reimand, J. *et al.* g:Profiler-a web server for functional interpretation of gene lists (2016 update). *Nucleic Acids Res* **44**, W83-89 (2016).
99. Hoelz, A., Debler, E. W. & Blobel, G. The Structure of the Nuclear Pore Complex. *Annual Review of Biochemistry* **80**, 613–643 (2011).
100. Vandesompele, J. *et al.* Accurate normalization of real-time quantitative RT-PCR data by geometric averaging of multiple internal control genes. *Genome Biology* **3**, research0034.1 (2002).
101. Perez-Riverol, Y. *et al.* The PRIDE database resources in 2022: a hub for mass spectrometry-based proteomics evidences. *Nucleic Acids Res* **50**, D543–D552 (2022).

Figure 1

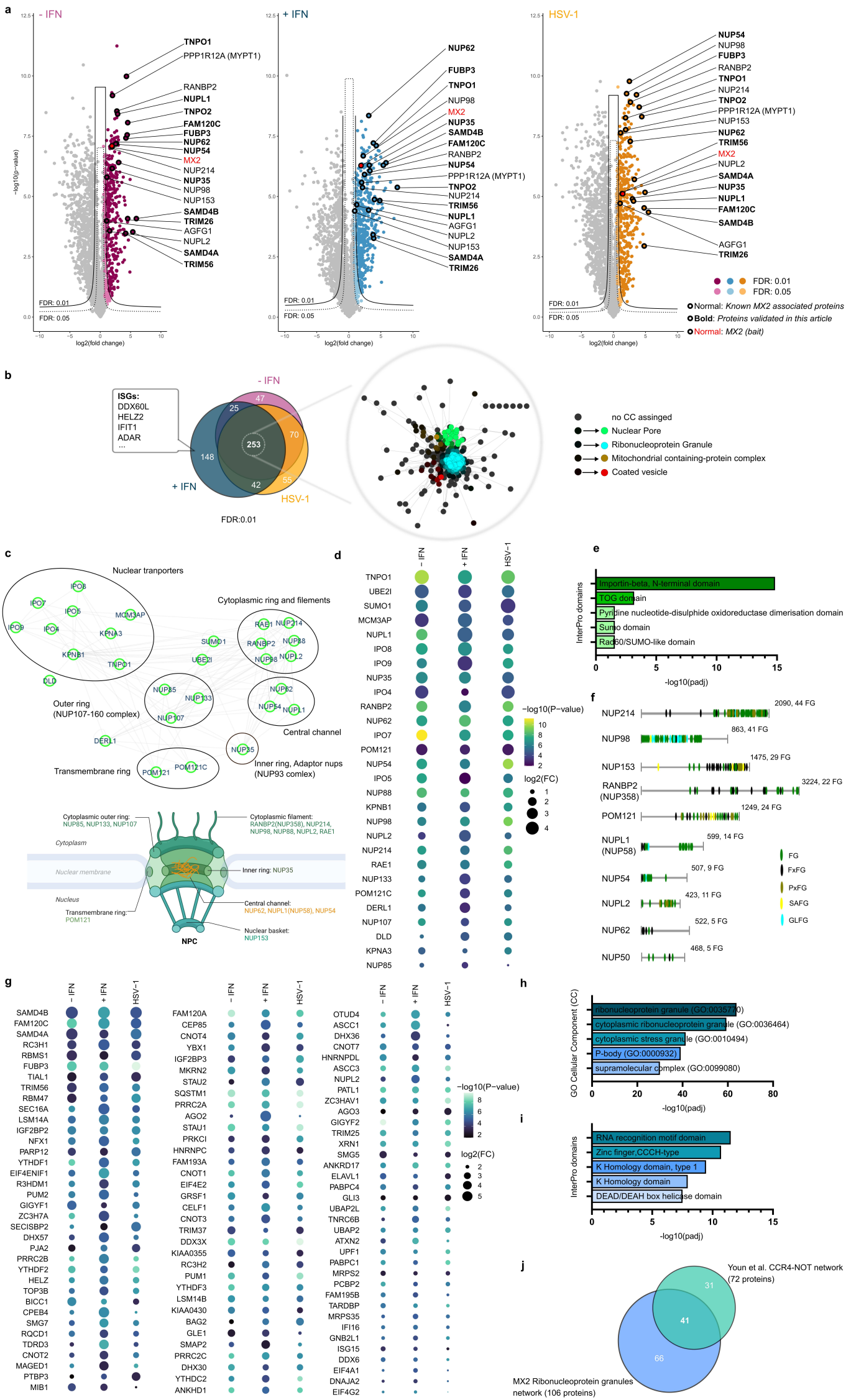
a
- IFN
+ IFN
HSV-1
−log10(p-value)
log2(fold change)
FDR: 0.01
FDR: 0.05
TNPO1
PPP1R12A (MYPT1)
RANBP2
NUPL1
TNPO2
FAM120C
FUBP3
NUP62
NUP54
MX2
NUP214
NUP35
NUP98
NUP153
SAMD4B
TRIM26
AGFG1
NUPL2
SAMD4A
TRIM56
Normal: Known MX2 associated proteins
Bold: Proteins validated in this article
Normal: MX2 (bait)
b
ISGs:
DDX60L
HELZ2
IFIT1
ADAR
...
- IFN
+ IFN
HSV-1
FDR:0.01
no CC assinged
Nuclear Pore
Ribonucleoprotein Granule
Mitochondrial containing-protein complex
Coated vesicle
c
Nuclear tranporters
Cytoplasmic ring and filements
Outer ring
(NUP107-160 complex)
Central channel
Transmembrane ring
Inner ring, Adaptor nups
(NUP93 comlex)
Cytoplasmic outer ring:
NUP85, NUP133, NUP107
Cytoplasmic filament:
RANBP2(NUP358), NUP214,
NUP98, NUP88, NUPL2, RAE1
Cytoplasm
Nuclear membrane
Nucleus
Inner ring: NUP35
Central channel:
NUP62, NUPL1(NUP58), NUP54
Transmembrane ring:
POM121
Nuclear basket:
NUP153
NPC
d
− IFN
+ IFN
HSV−1
−log10(P−value)
log2(FC)
e
InterPro domains
Importin-beta, N-terminal domain
TOG domain
Pyridine nucleotide-disulphide oxidoreductase dimerisation domain
Sumo domain
Rad60/SUMO-like domain
-log10(padj)
f
NUP214
2090, 44 FG
NUP98
863, 41 FG
NUP153
1475, 29 FG
RANBP2
(NUP358)
3224, 22 FG
POM121
1249, 24 FG
NUPL1
(NUP58)
599, 14 FG
NUP54
507, 9 FG
NUPL2
423, 11 FG
NUP62
522, 5 FG
NUP50
468, 5 FG
FG
FxFG
PxFG
SAFG
GLFG
g
− IFN
+ IFN
HSV−1
−log10(P−value)
log2(FC)
h
GO Cellular Component (CC)
ribonucleoprotein granule (GO:0035770)
cytoplasmic ribonucleoprotein granule (GO:0036464)
cytoplasmic stress granule (GO:0010494)
P-body (GO:0000932)
supramolecular complex (GO:0099080)
-log10(padj)
i
InterPro domains
RNA recognition motif domain
Zinc finger,CCCH-type
K Homology domain, type 1
K Homology domain
DEAD/DEAH box helicase domain
-log10(padj)
j
Youn et al. CCR4-NOT network
(72 proteins)
31
41
66
MX2 Ribonucleoprotein granules
network (106 proteins)

Figure 2

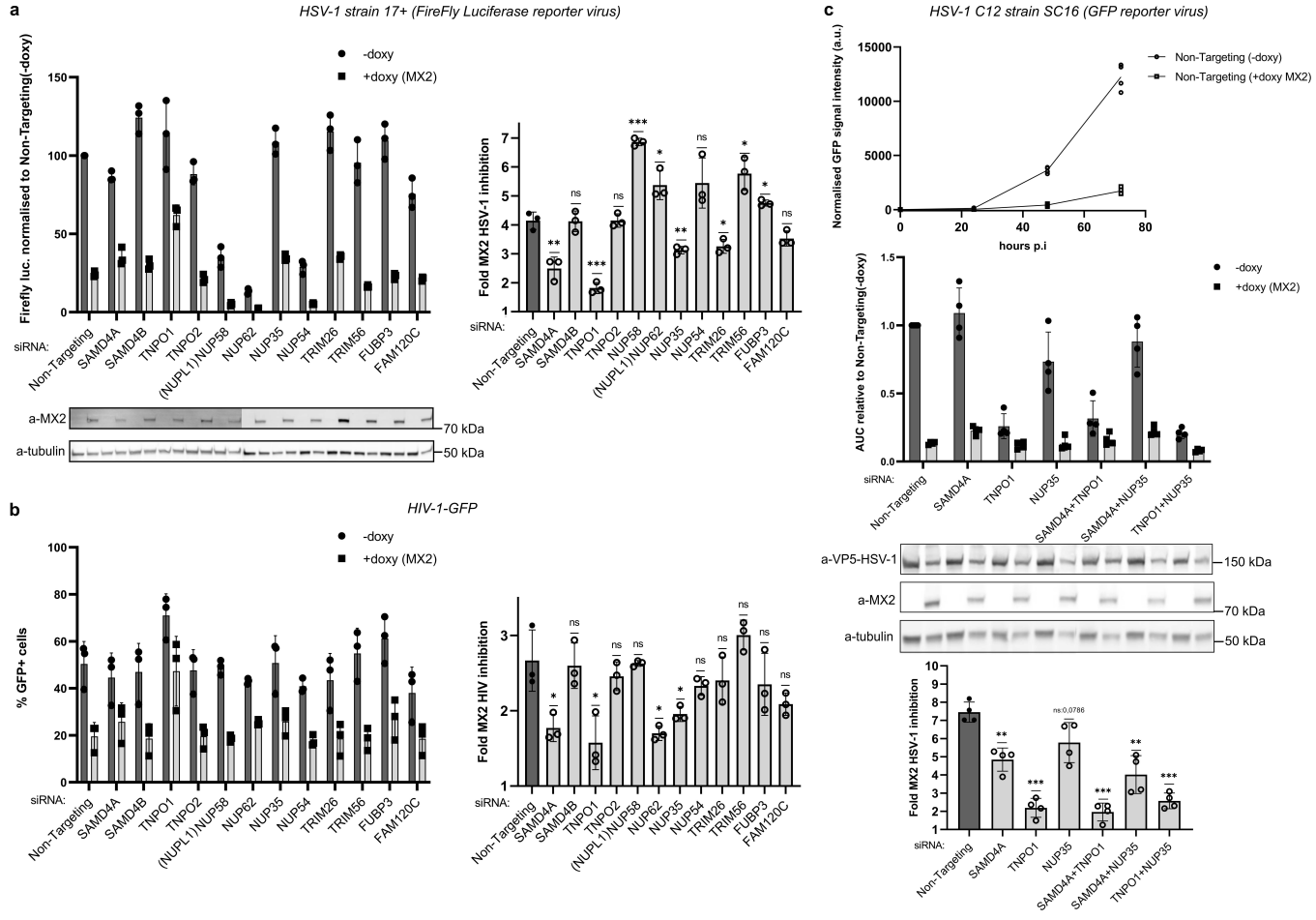
a
HSV-1 strain 17+ (FireFly Luciferase reporter virus)
-doxy
+doxy (MX2)
Firefly luc. normalised to Non-Targeting(-doxy)
siRNA:
Non-Targeting
SAMD4A
SAMD4B
TNPO1
TNPO2
(NUPL1)NUP58
NUP62
NUP35
NUP54
TRIM26
TRIM56
FUBP3
FAM120C
a-MX2
a-tubulin
70 kDa
50 kDa
Fold MX2 HSV-1 inhibition
b
HIV-1-GFP
% GFP+ cells
Fold MX2 HIV inhibition
c
HSV-1 C12 strain SC16 (GFP reporter virus)
Normalised GFP signal intensity (a.u.)
hours p.i
Non-Targeting (-doxy)
Non-Targeting (+doxy MX2)
AUC relative to Non-Targeting(-doxy)
SAMD4A+TNPO1
SAMD4A+NUP35
TNPO1+NUP35
a-VP5-HSV-1
150 kDa
ns:0.0786

Figure 3

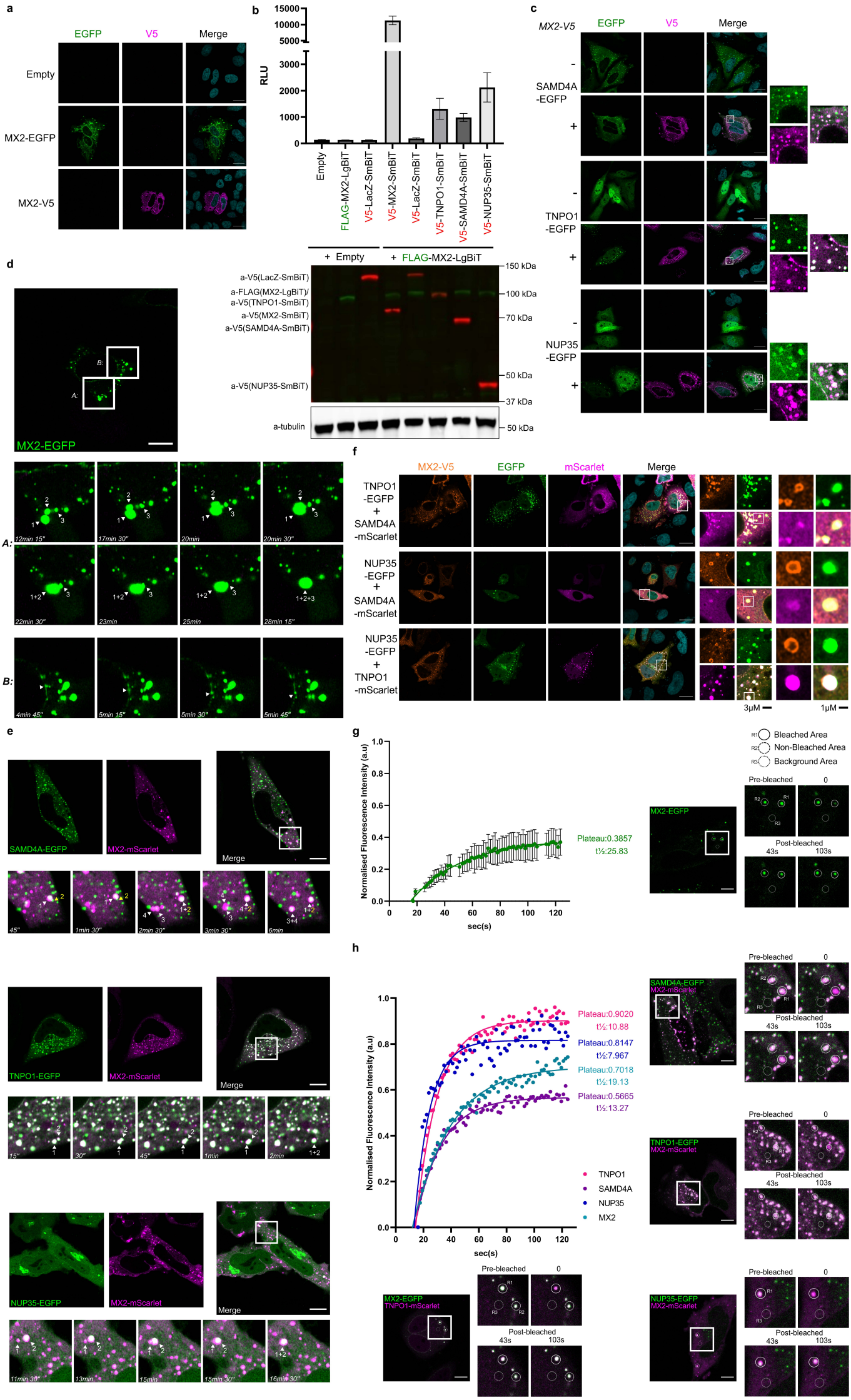
a
EGFP
V5
Merge
Empty
MX2-EGFP
MX2-V5
b
RLU
15000
10000
5000
3000
2000
1000
0
Empty
FLAG-MX2-LgBiT
V5-LacZ-SmBiT
V5-MX2-SmBiT
V5-LacZ-SmBiT
V5-TNPO1-SmBiT
V5-SAMD4A-SmBiT
V5-NUP35-SmBiT
c
MX2-V5
EGFP
V5
Merge
SAMD4A -EGFP
TNPO1 -EGFP
NUP35 -EGFP
d
B:
A:
MX2-EGFP
+ Empty
+ FLAG-MX2-LgBiT
a-V5(LacZ-SmBiT)
a-FLAG(MX2-LgBiT)/ a-V5(TNPO1-SmBiT)
a-V5(MX2-SmBiT)
a-V5(SAMD4A-SmBiT)
a-V5(NUP35-SmBiT)
a-tubulin
150 kDa
100 kDa
70 kDa
50 kDa
37 kDa
50 kDa
12min 15"
17min 30"
20min
20min 30"
22min 30"
23min
25min
28min 15"
4min 45"
5min 15"
5min 30"
5min 45"
f
MX2-V5
EGFP
mScarlet
Merge
TNPO1 -EGFP + SAMD4A -mScarlet
NUP35 -EGFP + SAMD4A -mScarlet
NUP35 -EGFP + TNPO1 -mScarlet
3μM
1μM
e
SAMD4A-EGFP
MX2-mScarlet
Merge
45"
1min 30"
2min 30"
3min 30"
6min
TNPO1-EGFP
MX2-mScarlet
Merge
15"
30"
45"
1min
2min
NUP35-EGFP
MX2-mScarlet
Merge
11min 30"
13min
15min
15min 30"
16min 30"
g
Normalised Fluorescence Intensity (a.u)
sec(s)
Plateau:0.3857
t½:25.83
Bleached Area
Non-Bleached Area
Background Area
Pre-bleached
Post-bleached
43s
103s
MX2-EGFP
h
Normalised Fluorescence Intensity (a.u)
sec(s)
Plateau:0.9020
t½:10.88
Plateau:0.8147
t½:7.967
Plateau:0.7018
t½:19.13
Plateau:0.5665
t½:13.27
TNPO1
SAMD4A
NUP35
MX2
SAMD4A-EGFP
MX2-mScarlet
TNPO1-EGFP
MX2-mScarlet
MX2-EGFP
TNPO1-mScarlet
NUP35-EGFP
MX2-mScarlet
Pre-bleached
Post-bleached
43s
103s

Figure 4

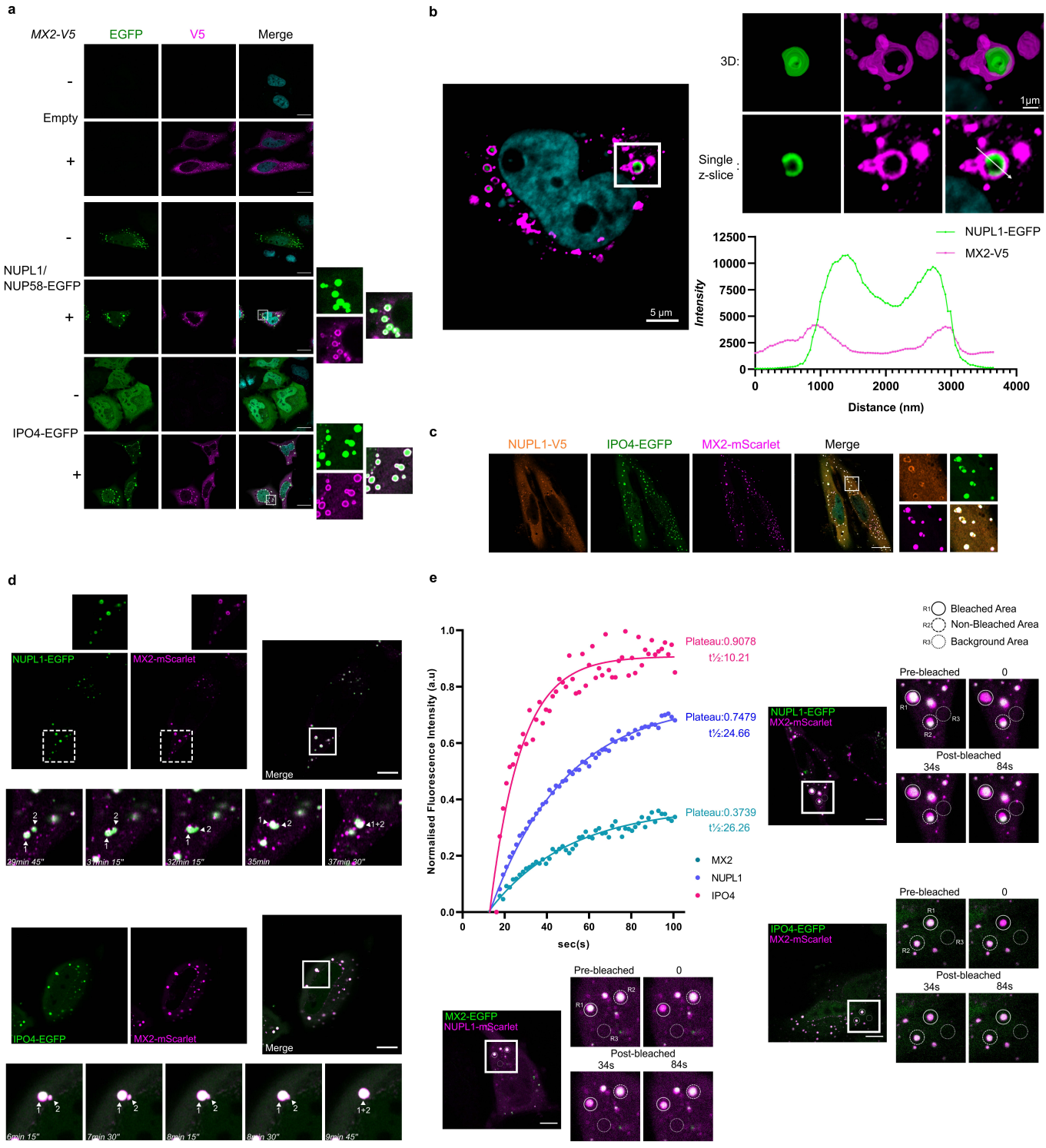
a
MX2-V5
EGFP
V5
Merge
-
Empty
+
-
NUPL1/
NUP58-EGFP
+
-
IPO4-EGFP
+
b
3D:
Single
z-slice
1µm
5 µm
NUPL1-EGFP
MX2-V5
Intensity
Distance (nm)
c
NUPL1-V5
IPO4-EGFP
MX2-mScarlet
Merge
d
NUPL1-EGFP
MX2-mScarlet
Merge
IPO4-EGFP
MX2-mScarlet
Merge
e
Normalised Fluorescence Intensity (a.u)
sec(s)
Plateau:0.9078
t½:10.21
Plateau:0.7479
t½:24.66
Plateau:0.3739
t½:26.26
MX2
NUPL1
IPO4
Bleached Area
Non-Bleached Area
Background Area
Pre-bleached
Post-bleached
NUPL1-EGFP
MX2-mScarlet
IPO4-EGFP
MX2-mScarlet
MX2-EGFP
NUPL1-mScarlet

Figure 5

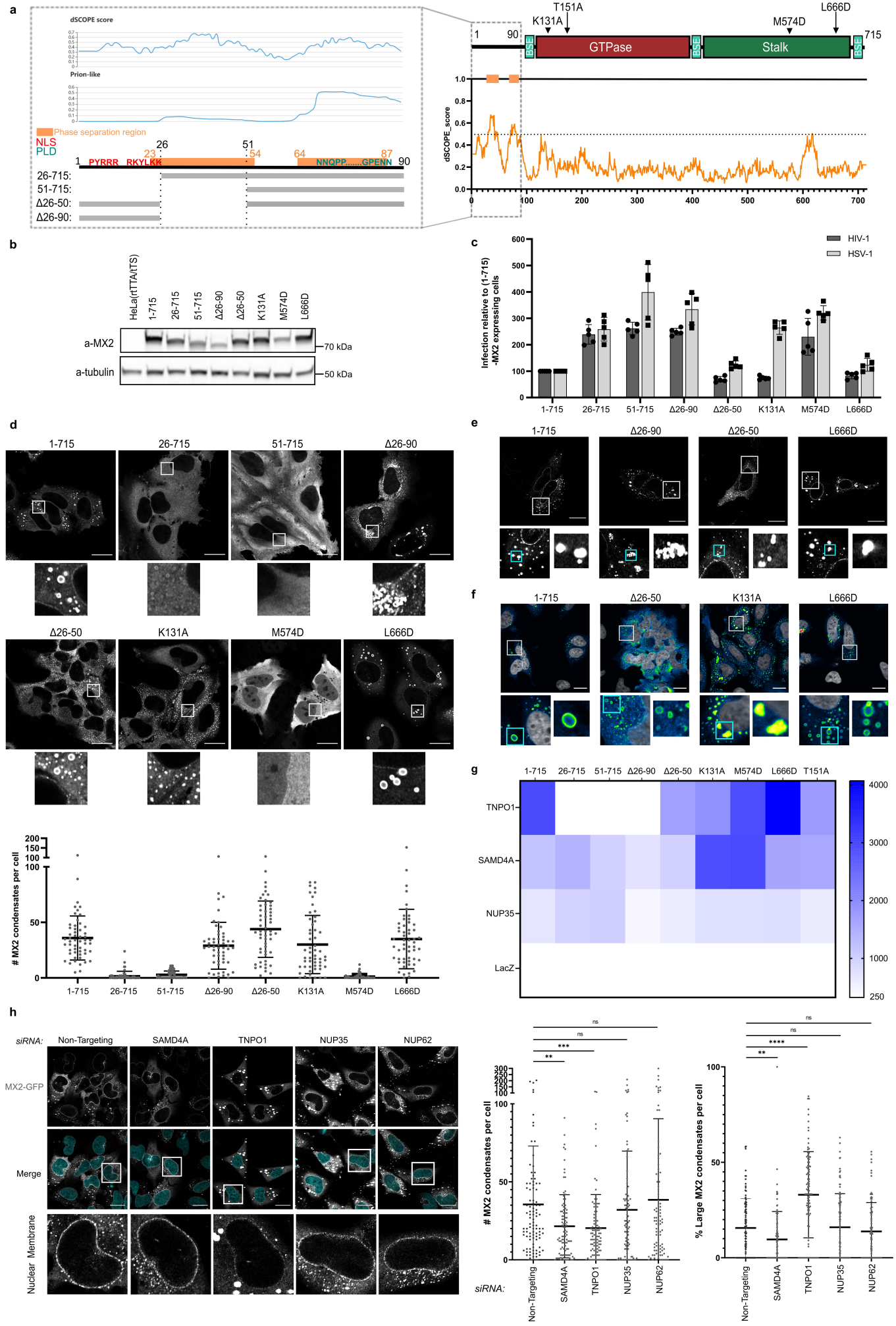
a
dSCOPE score
Prion-like
Phase separation region
NLS
PLD
1 PYRRR RKYLKK NNQPP.....GPENN 90
26-715:
51-715:
Δ26-50:
Δ26-90:
T151A
K131A
M574D
L666D
GTPase
Stalk
dSCOPE_score
b
HeLa(rtTTA/tTS)
1-715
26-715
51-715
Δ26-90
Δ26-50
K131A
M574D
L666D
a-MX2
a-tubulin
70 kDa
50 kDa
c
HIV-1
HSV-1
Infection relative to (1-715) -MX2 expressing cells
d
e
f
g
TNPO1
SAMD4A
NUP35
LacZ
T151A
MX2 condensates per cell
h
siRNA:
Non-Targeting
SAMD4A
TNPO1
NUP35
NUP62
MX2-GFP
Merge
Nuclear Membrane
% Large MX2 condensates per cell

Figure 6

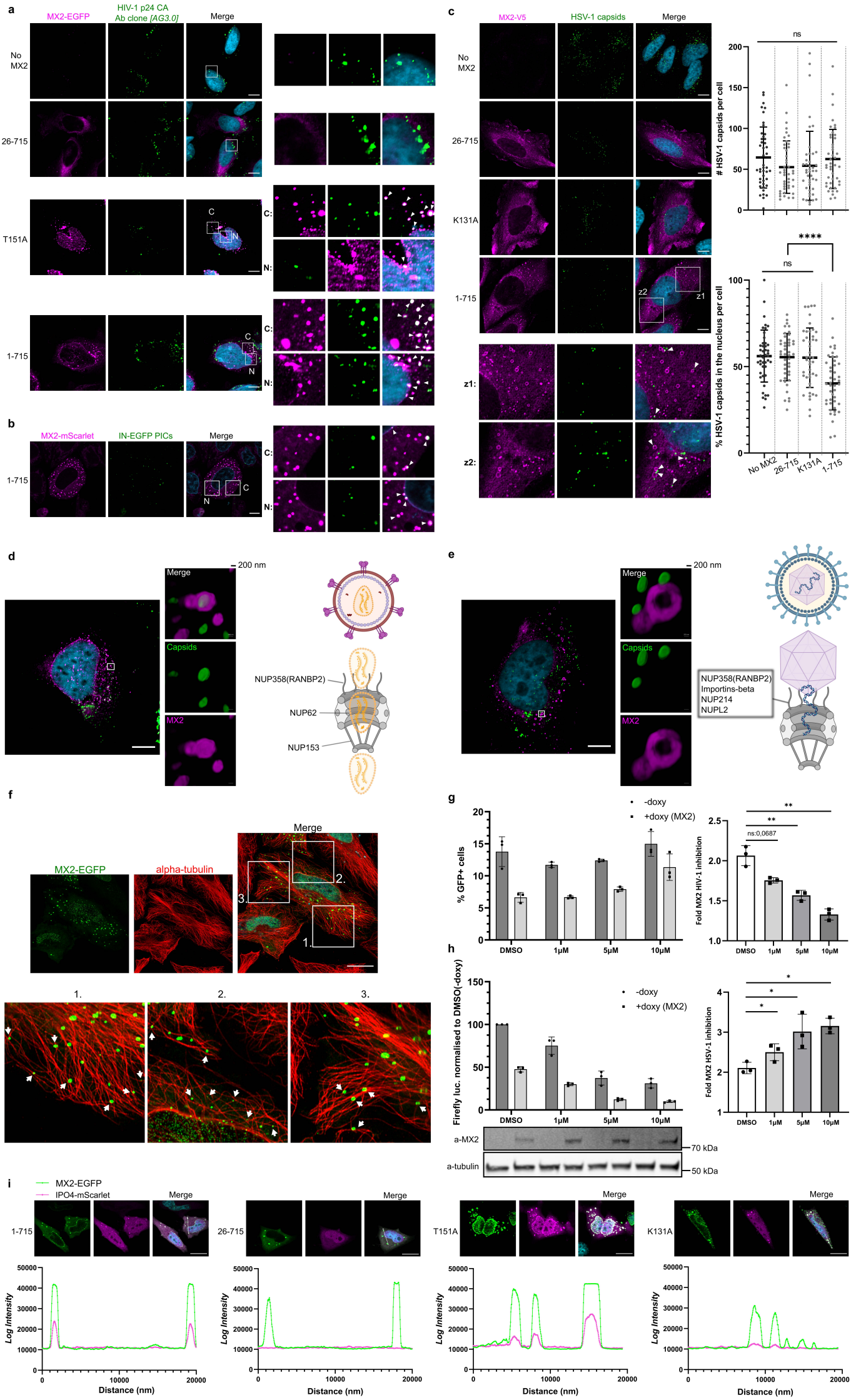
a
MX2-EGFP
HIV-1 p24 CA Ab clone [AG3.0]
Merge
No MX2
26-715
T151A
1-715
C:
N:
b
MX2-mScarlet
IN-EGFP PICs
Merge
1-715
c
MX2-V5
HSV-1 capsids
Merge
No MX2
26-715
K131A
1-715
z1:
z2:
HSV-1 capsids per cell
% HSV-1 capsids in the nucleus per cell
ns
****
No MX2
26-715
K131A
1-715
d
200 nm
Merge
Capsids
MX2
NUP358(RANBP2)
NUP62
NUP153
e
200 nm
Merge
Capsids
MX2
NUP358(RANBP2)
Importins-beta
NUP214
NUPL2
f
MX2-EGFP
alpha-tubulin
Merge
1.
2.
3.
g
-doxy
+doxy (MX2)
% GFP+ cells
DMSO
1μM
5μM
10μM
Fold MX2 HIV-1 inhibition
ns:0,0687
h
Firefly luc. normalised to DMSO(-doxy)
Fold MX2 HSV-1 inhibition
a-MX2
a-tubulin
70 kDa
50 kDa
i
MX2-EGFP
IPO4-mScarlet
Merge
1-715
26-715
T151A
K131A
Log Intensity
Distance (nm)